Materials Chemistry and Physics 219 (2018) 493–511

Contents lists available at ScienceDirect

Materials Chemistry and Physics

journal homepage: www.elsevier.com/locate/matchemphys

Corrosion and anodizing behaviour of friction stir weldment of AA2198-T851 Al-Cu-Li alloy

Uyime Donatus[a,*], Raphael Oliveira Ferreira[b], Naga Vishnu Vardan Mogili[c], Barbara Victoria Gonçalves de Viveiros[a], Mariana Xavier Milagre[a], Isolda Costa[a]

[a] Instituto de Pesquisas Energéticas e Nucleares, Av. Prof. Lineu Prestes, 2242, São Paulo, SP, Brazil
[b] Escola Politécnica da Universidade de São Paulo, Av. Prof. Mello Moraes, 2463, São Paulo, SP, Brazil
[c] Centro Nacional de Pesquisas em Energia e Materiais (CNPEM), Laboratório Nacional de Nanotecnologia (LNNano), Rua Giuseppe MaximoScolfaro 10.000, 13083-100, Campinas, SP, Brazil

HIGHLIGHTS

- Polishing affects the corrosion of AA2198 alloy friction stir weldment.
- Severe localized corrosion morphology differ with surface finish.
- Varying anodic oxide layer thicknesses form across the weldment after anodizing.
- There is a reversal in microhardness values across the weldment after anodizing.

ARTICLE INFO

Keywords:
Aluminium alloy
Friction stir welding
Anodizing
Pitting corrosion
Near surface deformed layer

ABSTRACT

Anodizing behaviour of AA2198-T851 friction stir weldment and the corrosion behaviour of unpolished and polished weldments of the alloy have been investigated. Electrochemical and microscopic techniques were employed in the study. The results revealed that the manufacturing-process induced near-surface deformed layer significantly affected the corrosion behaviour of the weldment. Thus, the corrosion behaviour of the weldment in the polished condition (which is the common practice) was different from that of the unpolished one due to the presence of near-surface deformed layer. Anodizing as a corrosion protection method for the weldment caused the formation of pronounced non-uniform oxide layer thicknesses across the weld zones. This was because the weldment oxidized at a higher rate compared with the parent material (PM) due to an increased proportion of Li in solid solution in the stir zone of the weldment.

1. Introduction

The understanding of the corrosion behaviours of friction stir weldments of Al alloys has been of research interest for over 10 years ever since the invention of the friction stir welding process in 1991 [1]. Reports in the literature indicate that the corrosion susceptibilities of friction stir weldments of Al alloys are unpredictable. A change in temper condition [2,3] and welding parameters [4–6] can significantly alter the corrosion susceptibility of the friction stir weldment of an Al alloy. Thus, every case needs to be treated differently, and a general prediction should not be made for weldments of Al alloys even if they are from the same series and are alloys of the same composition especially since temper conditions and welding parameters affect corrosion susceptibility and behaviour.

Further, investigations on the corrosion behaviours of friction stir weldments of Al alloys are mostly carried out using mechanically abraded/polished weldments and are rarely carried out on weldments that are not mechanical abraded or polished [2,4,7–14]. However, the corrosion behaviour of an unpolished weldment can be very different after polishing, especially the kinetics of the most susceptible regions as will be revealed in this study. It is well established that most wrought Al alloys have near-surface deformed layers (NSDLs) that were created at the near-surface of the alloys during production processes (such as rolling, extrusion and machining) due to severe preferential deformation at the surfaces of the alloys during these processes [15–19]. In many cases, the near-surface deformed layer or altered surface layer exhibits a very different corrosion behaviour compared with the underlying bulk alloy [19]. Consequently, the overall corrosion behaviour

* Corresponding author.
E-mail address: uyimedonatus@yahoo.com (U. Donatus).

https://doi.org/10.1016/j.matchemphys.2018.08.053
Received 4 June 2018; Received in revised form 3 August 2018; Accepted 19 August 2018
Available online 22 August 2018
0254-0584/

of the alloy is affected. Thus, if the NSDL influences the corrosion behaviour of the bulk alloy, it will inevitably have effects on the friction stir weldments of the alloy. Interestingly, this is not often taken into consideration in studies involving characterization of the corrosion behaviours or susceptibilities of friction stir weldments, or even other forms of weldments in general [4,5,7,11,13,20].

It is important to state that mechanical abrasion and/or polishing introduces a different type of altered surface layer and caustic etching might be required for complete removal. However, caustic etching is not appropriate for weldments since the zones could be etched at different rates. In addition, it can also cause the preferential dissolution of some regions. Thus, in this work, a friction stir weldment of the AA2198-T851 alloy has been used to show that the manufacturing process induced NSDL has a significant influence on the corrosion behaviour of the weldment; and this was done by comparing a polished weldment with an unpolished weldment.

The AA2198-T851 alloy is a new generation Al-Li alloy suitable for use in the aerospace industry. As a heat treatable aluminium alloy, the AA2198-T851 alloy shows pronounced metallurgical variations across the various zones in its friction stir weldment. These variations are mostly associated with the distribution, coarsening, redistribution and reprecipitation of the strengthening precipitates in the heat affected zone (HAZ), thermo-mechanically affected zone (TMAZ) and stir zone (SZ) [21–25]. The metallurgical variations between the zones can cause preferential corrosion susceptibilities and promote galvanically enhanced dissolution of the most active regions. Interestingly, the AA2198 alloy, being an Al-Cu-Li alloy, can have one or a combination of the T_1 (Al_2CuLi), θ (Al_2Cu), δ' (Al_3Li) and S'(Al_2CuMg) strengthening phases depending on the thermomechanical treatment [25]; and these phases can even occur as composite structures within the matrix of the alloy [26]. For the T851 temper considered in this work, the T_1 phase is the most dominant phase in the parent metal (PM) [27–29], and it is the phase of interest with respect to the mechanical and corrosion behaviours of the new generation Al-Cu-Li alloys. However, this phase may not be predominant in the other zones of the weld, such as the SZ which usually comprise different phases compared with the TMAZ, HAZ and PM. Thus, in addition to the corrosion susceptibilities of the individual regions, macro-galvanic coupling can be induced in the weldment when placed in an enabling environment. Further, the presence or absence of the near-surface deformed layer, with a different metallurgical composition, on the surfaces of the PM and HAZ also plays a role in increasing or decreasing the effect of the macro-galvanic coupling. It should be noted that the deformation introduced by friction stir welding in the TMAZ/SZ due to the action of the tool shoulder is different from the NSDL introduced on the PM and HAZ during the fabrication process of the alloy. In this work, the emphasis is on the latter.

As already mentioned, the evolution of corrosion in the friction stir weldment of the AA2198-T851 alloy, when it is placed in an enabling environment, is highly unavoidable. It is, therefore, necessary to protect the weldment from corrosion. Anodizing has been the most used method for the protection of Al and its alloys. Surprisingly, only a few reports on anodizing of friction stir weldments of Al alloys exist in the literature [22,23,30,31]. The anodizing behaviour of friction stir weldments of dissimilar Al alloys has been previously reported by Ref. [22]. In this work, it was said that the parent materials of a dissimilar friction stir weldment of AA5083-O and AA6082-T6 alloys were the most oxidized regions compared with the TMAZ and SZ during anodizing. Efforts were made to understand the reasons for the differential oxidation rates across the weld zones. Particle distributions, compositional variations, grain sizes and barrier layer thicknesses were considered. There was a slight correlation with barrier layer thicknesses across the zones, but the core reason for the disparity was not established. This was probably because the weld was dissimilar and a direct correlation between the differential rate of oxidation of the weld zones with the factors considered was difficult. However, a method was developed to minimise the differential rates of oxidation across the weld zones during anodizing. The technique involved sputter deposition of pure Al on the weldment before anodizing. The success of the method [23] indicated that the differential oxidation on the weldment was due to the zonal heterogeneities across the surface of the weldment. The overall uniformity in the anodizing response across the weldment with prior sputter deposition was more of a factor of the degree of uniformity of the surface exposed to the anodizing solution than the sub-surface characteristics of the weldment. Recently, Dick et al. [30] also investigated the effect of friction stir welding on the anodizing behaviour of the AA7050 alloy. They concluded that the oxide layer formed during sulphuric acid anodizing was 25% thinner on the SZ and 25% thicker on the TMAZ and heat affected zone (HAZ). The variations observed were associated with differences in hardness values across the zones. The TMAZ and HAZ with lower hardness values had higher oxide layer thicknesses compared with the SZ which had higher hardness values on the average. Thus, they revealed that the higher the hardness (due to the presence of strengthening precipitates), the thinner the oxide layer. On the contrary, this was not the case in the work reported by other authors [22]: the weld zones with lower hardness values formed lower porous oxide layer thicknesses compared with the PM side of the AA6082 alloy, which had the highest hardness values. In fact, the thickness range of the porous oxide layer formed on the SZ (which had about the lowest hardness values) of the dissimilar friction stir weldment was about the lowest compared with those of the other weld zones. Thus, it is essential to further investigate the differential oxide layer formation on the different zones of friction stir weldments of Al alloys, mainly as this will affect the in-service performance of the weldments.

This work highlights the influence of the NSDL on the corrosion behaviour of the friction stir weldment of a new generation Al-Cu-Li alloy. It also sheds more light on the anodizing behaviour of the weldment and reveals the inverse relationship between the microhardness values across the surface of the weldment before and after anodizing. To the best of authors' knowledge, the cases of NSDL effect on the corrosion behaviour of Al weldments and the inverse relationship of the microhardness values before and after anodizing are reported here for the first time.

2. Experimental

Friction stir weldment of AA2198-T851 alloy (Al-3.31Cu-0.96Li-0.31Mg-0.04Fe-0.03Si-0.25Ag-0.4Zr (wt. %)) prepared using a tool with a shoulder diameter of 6 mm, pin diameter of 2 mm, penetration of 1.9 mm at a rotation speed of 800 rpm and traverse speed of 150 mm/min was employed in this study.

Samples for the examination of grain sizes and morphologies were polished up to 1 μm surface finish and etched in a solution comprising 2% hydrofluoric and 25% nitric acid for 10 s. The sample used for the particle distribution examination was not etched.

Vickers microhardness values were obtained from the PM in the AS of the weldment to the SZ using a load of 0.3 kg for a dwell time of 10 s. The measurements were obtained across the surfaces of the anodized and un-anodized weldments. Three sets of measurements were obtained and averaged for each weldment.

Agar gel corrosion visualization test method was employed for corrosion studies on un-anodized weldments. The test was carried out on an unpolished weldment (with manufacturing-process induced near-surface deformed layer - denoted as + NSDL in this work) and polished weldment (with no manufacturing-process induced near-surface deformed layer - indicated as -NSDL in this work). The –NSDL sample was prepared by sequentially grinding and polishing the samples up to 1 μm surface finish using SiC papers and diamond pastes. A surface layer of about 50 μm was removed during the grinding and polishing process. Agar gel was prepared by adding 1.5 g of agar powder and 3.75 mL of phenolphthalein (1% w/v) to a boiling 3.5% NaCl solution. The solution was cooled to a viscous state prior to deposition on the +NSDL and

-NSDL weldments. Optical images were obtained over time in accordance with noticeable changes in colour across the weldments. It should be noted that in the presented results of the agar gel corrosion visualization test, pink regions represent areas of macro cathodic activities generating OH^- while colourless regions represent areas of zero activity or anodic activities.

Potentiodynamic polarization tests were conducted using a three-electrode set-up comprising the working electrode, a platinum counter electrode and a Ag/AgCl (saturated KCl) reference electrode. The solution employed was 3.5% NaCl solution acidified by adding 10 mL of HCl (35%) to a pH of 2.29. The solution is designated as A-3.5% NaCl solution in this study. An EC-Lab Bio-Logic potentiostat and a cell designed to expose 0.025 cm^2 were used for the potentiodynamic polarization tests. An O-ring with a diameter of 0.162 mm was used to define the exposed surface area. However, for anodized samples, the exposed surface area was 1 cm^2 in order to obtain representative measurements. Prior to the potentiodynamic polarization measurements, open circuit potential measurement was carried out for 30 min. A scan rate of 1 mV/s was employed, and the measurements were obtained from −200 mV vs OCP.

Anodizing was carried out in 4 M H_2SO_4 solution using two methods: a constant-voltage or potentiostatic anodization at 14 V for 600 s, and potentiodynamic anodization to 12 V from open circuit potential using a scan rate of 16.67 mV/s. In both cases, anodizing was carried out on both, the base material (separately) and on the friction stir weldment comprising all the zones. Anodizing was carried out using a Solatron potentiostat. The exposed surface area was 6 cm^2 (with a width of 1.5 cm and a length of 4 cm measured from the PM in the advancing side (AS) to the PM in the retreating side (RS) at equal distances from the weld centre). Beeswax was used to coat the samples.

A JEOL JSM-6010LA scanning electron microscope equipped with an energy dispersive x-ray spectroscopy (EDS) detector and a JEOL JEM 2100 transmission electron microscope were used for microstructural characterization. TEM samples were prepared by twin-jet electropolishing technique using a solution comprising 35% HNO_3 in methanol at - 20 °C. Prior to electropolishing, the samples were sequentially ground to a thickness in the range of 100 μm. Following this, 3 mm discs were cut from the sample and then placed in Struers Tenupol holder for electropolishing. TEM sample for NSDL cross-sectional examination was prepared using focus ion beam (out-lift) method on an FEI Helios microscope. The surface of the sample was protected with Pt-based coating prior to focus ion beam thinning. High-angle annular dark-field – scanning transmission electron microscopy (HAADF-STEM) analysis was also conducted.

3. Results and discussion

3.1. Microstructure and corrosion susceptibility

3.1.1. General microstructure

The main microstructural features of the zones in the friction stir weldment of the AA2198-T851 alloy studied are presented in Figs. 1 and 2. Displayed in Fig. 1 are the optical micrographs of the surface (Fig. 1(a)–(c)) and the cross-section (Fig. 1(d)–(f)) of the weld zones showing the variations in grain sizes and morphologies across the weld zones.

There were no observable changes in the average grain sizes and grain morphology in the PM and HAZ of the weldment of the alloy, and this is typical for most age hardened Al alloys. The grains are large and equiaxed across the surfaces of these zones and elongated in the direction of working when observed from the cross-section. In age-hardenable Al alloys, the microstructural differences between the PM and HAZ are often due to those from processes like coarsening/dissolution of strengthening precipitates and rearrangement of dislocations, but not changes in grain size. The TMAZ is composed of highly deformed grains and fragmented grains of the PM since this region experienced both mechanical deformation and high temperature (but not high enough to cause recrystallization); whereas the SZ is composed of dynamically recrystallized ultrafine grains which resulted from intense deformation and temperatures high enough to cause recrystallizaton.

Fig. 2 displays the scanning electron and transmission electron micrographs of the PM (Fig. 2(a) and (b)) and the SZ (Fig. 2(c) and (d)), respectively. From the SEM images, coarse Cu-Fe rich intermetallic particles were observed in both regions; however, the particles were finer in the SZ, owing to the fact that they had been mechanically fragmented, and were evenly distributed. Nonetheless, finer particles (that are most likely T_B (Al_7Cu_4Li) particles [32]) were also uniformly distributed in the SZ of the weld, as shown in the inset in Fig. 2(c). These were not observed in the other zones of the weldment. On the other hand, TEM images show that the PM contained a high volume fraction of T1 phase which was difficult to find in the SZ. (TEM analyses confirming that the particles in the PM (Fig. 2(b)) are indeed the T1 phase are presented elsewhere [27–29]). Thus, T1 particles dissolved as the weld centre was approached and were wholly dissolved in the SZ. The conditions were not favourable for re-precipitation of the peak-aged or near peak aged T1 particles afterwards. However, this resulted in reprecipitation of particles suspected to be T_B (as shown in the inset in Fig. 2(c)). The temperature reached in the SZ during welding is usually above 450° C [25]. This causes rapid dissolution of T1 particles that were initially in this region. After welding, the material cools rapidly to room temperature. This does not favour T1 re-precipitation. To have the re-precipitation of T1 particles in this zone, artificial aging at holding temperatures above 130 °C will be necessary [33]. At temperatures below this, it is the precipitation of GP zones and δ' phases that is favoured [33]. Similar findings were reported in the literature for most Al-Cu-Li weldments. Chen and Chaturvedi [32] revealed that the T1 precipitates dissolved while the T_B precipitates formed at different temperatures in simulated HAZs of an AA2195-T8 alloy. Likewise, De Geuser et al. [34] also reported that the high temperature experienced in the weld nugget of an AA2050 friction stir welded alloy resulted in the complete dissolution of the pre-existing strengthening phases that were predominantly T1 particles. Fonda and Bingert [35] also presented similar findings for the AA2195 friction stir weldment. Further, the dissolution of T1 particles and the precipitation of T_B particles in the SZ of the friction stir weldment of an AA2198 alloy has also been reported [36]. Given that the T1 phase is the most influential precipitate, in terms of mechanical and electrochemical responses, for the new generation Al-Cu-Li alloys, the variations in the volume fractions of the T1 and T_B will undoubtedly affect the mechanical and electrochemical responses of the friction stir weldment of the AA2198-T851 alloy.

Microstructural characterization of the NSDL was also carried out. Presented in Fig. 3 are SEM-EDS maps of the unpolished surface of the AA2198-T851 alloy. The observed magnesium-rich bands, alongside parallel groves and micro-cracks, are typical features of the near-surface deformed layers on Al alloys.

The TEM images presented in Fig. 4 also show the typical features of the near-surface deformed layer on the AA2198-T851 alloy. From the EDS maps (Fig. 5) of a selected region of the image in Fig. 4(a), it is also clear that the near-surface deformed layer is composed of an outermost oxide layer that is rich in Mg and Si.

In an on-going work, it has also been revealed that this region is enriched in Li. Li was not shown in the maps because EDS does not detect Li. In the TEM analysis (Figs. 1–5) are used to represent the Cu-rich particles observed beneath the outermost oxide layer, whilst I, II, and III are used to represent the ultrafine grains beneath the oxide layer. This means that in addition to the oxide layer, the NSDL is also composed of Cu-rich particles and ultrafine grains. (The Cu and Fe detected on the Pt coating were from the sample preparation process). Clearly, there is an apparent compositional mismatch between the NSDL (particularly the outermost region) and the underlying bulk alloy.

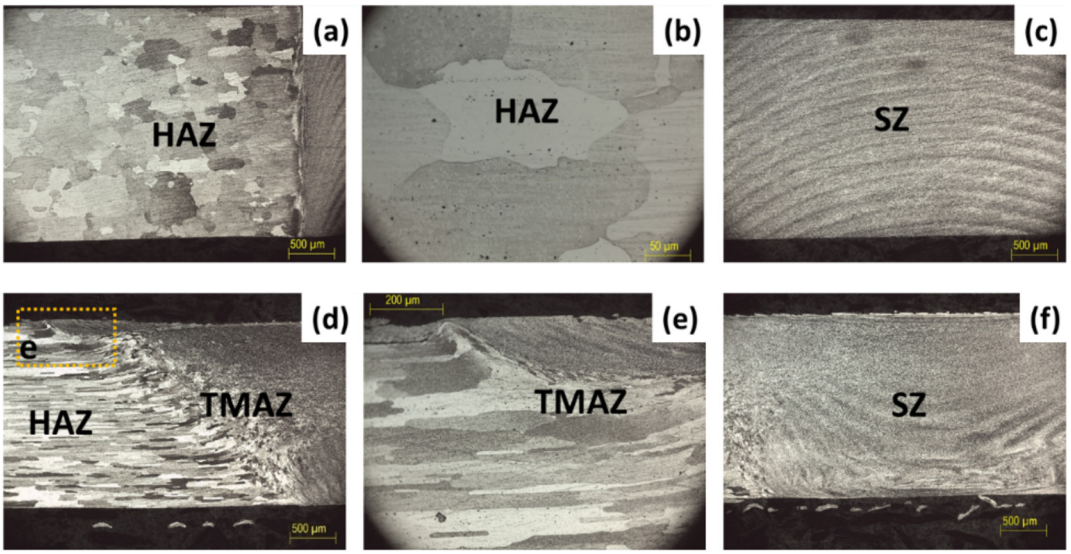

Fig. 1. Optical micrographs obtained from the surface and cross-section of the AA2198-T851 friction stir weldment.

These distinct features cause marked differences in the electrochemical behaviours of the NSDL and the underlying bulk alloy as will be revealed in the sections below.

3.1.2. Corrosion susceptibility of +NSDL and –NSDL weldments

Presented in Figs. 6 and 7 are the optical images of the +NSDL and –NSDL weldments during the early and later hours of the agar gel visualization test. The images of the +NSDL weldment are presented on the left whilst those of the –NSDL weldment are displayed on the right.

Upon the deposition of agar gel, the weldments showed no evidence of corrosion activities within the first 2 min, both on the + NSDL (Fig. 6(a)) and on the –NSDL (Fig. 6(b)) weldments. However, discontinuous dark features were observed on the AS of the weld as indicated by the blue arrow in Fig. 6(a). These features were not caused by corrosion as they were inherent in the material (this is discussed later in this section). Nonetheless, in less than an hour, corrosion

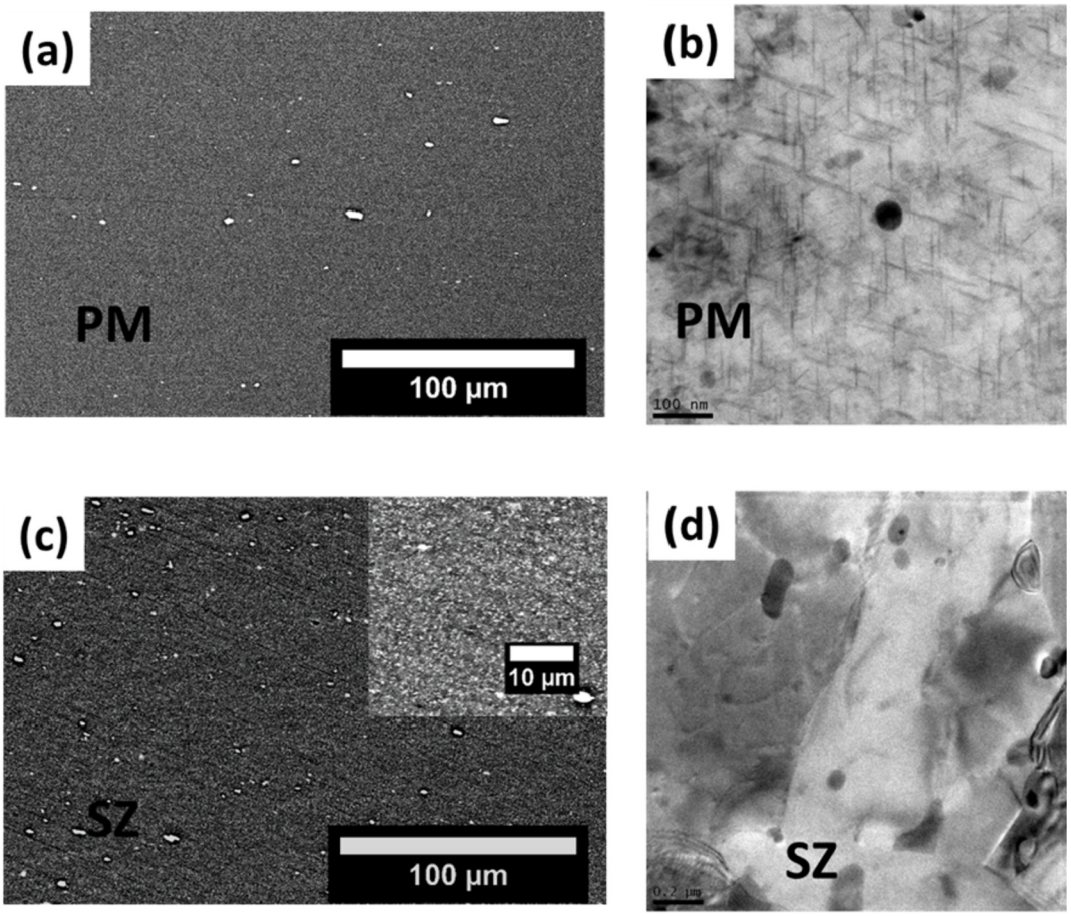

Fig. 2. Scanning electron micrographs and bright field transmission electron micrographs of the ((a) & (b)) PM and ((c) & (d)) SZ.

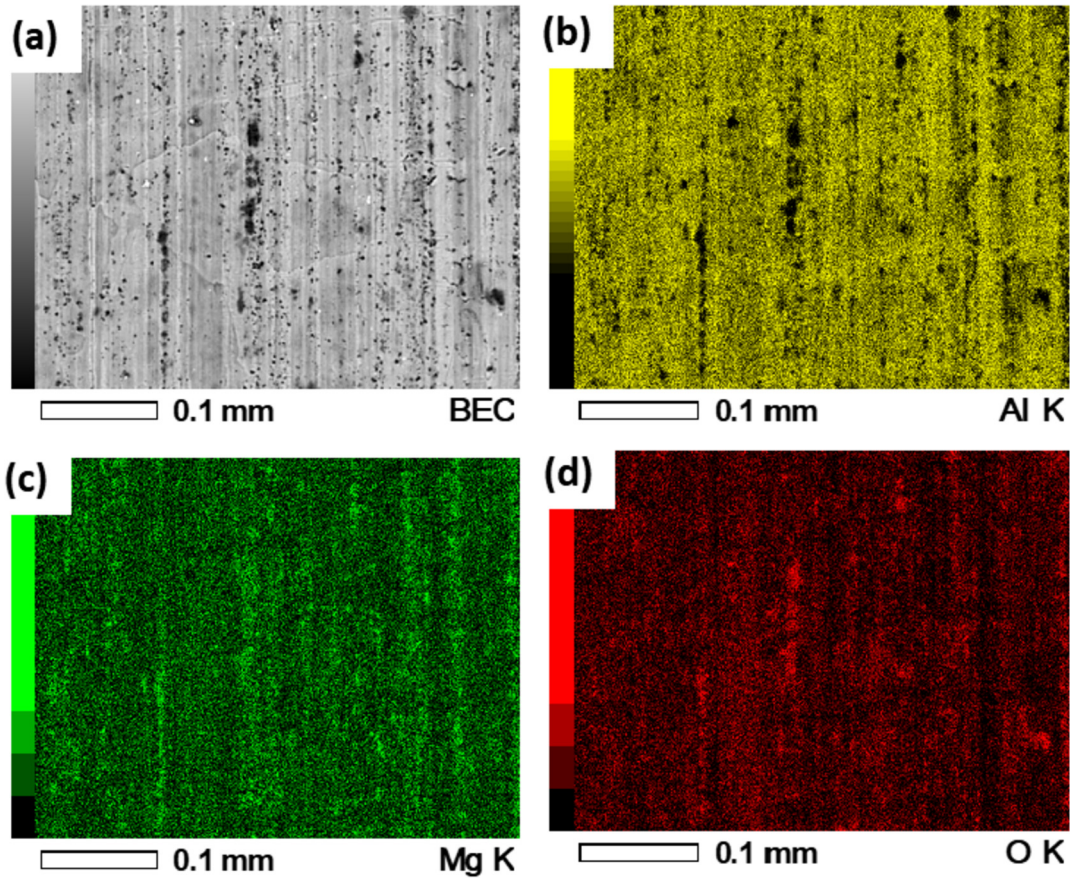

Fig. 3. (a) Scanning electron micrograph of the unpolished parent material of the AA2198-T851 alloy. ((b)–(e)) EDS maps of the demarcated region in (a) showing the major compositions of the bands.

activities were observed. The activities were mainly on the polished (-NSDL) weldment but sparingly on the unpolished (+NSDL) weldment, and this became pronounced after 1 h, as shown in Fig. 6(c) and (d). The weld region was apparently the most resistant to corrosion, with the cathodic reaction of O_2 reduction that generates OH^- predominating the entire weld region of the polished weldment. For the unpolished weldment, the TMAZ region just outside the weld appeared to be the most corrosion resistant, at least within the first 2 h of the test. Also, within the first 2 h, hydrogen bubbles were observed on the PM side of the -NSDL weldment, as indicated by the red arrow; and the cathodic activities were noticeably intense, spreading more into the TMAZ of the AS. The highly localised evolution of hydrogen bubbles indicated that severe localized corrosion (SLC) had already begun in this region of the polished weldment.

Further, in the later hours of corrosion test (Fig. 7), from 8 h to 24 h, cathodic activities had spread from the TMAZ of the RS across the weld to the PM in the AS for the +NSDL weldment, and bubbles were also observed on the PM side in the RS. Although hydrogen evolution is not always an evidence of severe localised corrosion in this alloy, in this case, the highly localised hydrogen evolution spots were a clear indication of severe localized corrosion. Our experience with this alloy has shown that for an unpolished AA2198-T851 alloy with manufacturing-process induced near-surface deformed layer, severe localized corrosion does not readily occur in this environment (at least not within 8 h of exposure) except if triggered galvanically by the presence of an active macro cathodic region. The primary active macro cathodic regions, in this case, are the weld, the TMAZ, and the lumps of cathodic particles deposited in the AS of the weld. The PM sides of both weldments were the regions most susceptible to corrosion, and this is down to the fact that the active T1 (Al_2CuLi) phase is heavily present in the PM. The T1 phase is rarely found in the SZ. However, the intensity of the severe localized corrosion in the PM side of the +NSDL weldment was not as pronounced as that of the PM side of the –NSDL weldment. Interestingly, the SLC morphology in the -NSDL weldment was very different from that in the +NSDL weldment. In the polished weldment, a central pitting site was initiated in less than 2 h of corrosion test. This central (primary) pit developed with time, without the formation of new SLC sites. However, after about 8 h, other secondary SLC pits were observed in the vicinity of the central pit, and were formed in a ring-like manner around this central pit. The pH around the central pit was low, and the difference in pH between the susceptible region and the adjacent uncorroded region was higher compared with that in the +NSDL weldment. Also, it is most likely that the chloride concentration in the SLC region was higher compared with the other part. This is because cations (Al^{3+} and H^+) are generated in SLC regions/pits, and this usually results in Cl^- ions ingress for electroneutrality. These factors promote local depassivation and encourage the ready dissolution of the matrix and hydrogen evolution. Like the case of the central pit, the appearance of the secondary SLC pits was preceded by the evolution of hydrogen bubbles. As mentioned earlier, the SLC morphology in the PM side of the +NSDL weldment was different. In this weldment, the pH difference between the susceptible region and the adjacent region was lower (compared with the polished weldment), and there was no central pit surrounded by secondary pitting sites in a ring-like version. The pits were spread all over the susceptible PM region, and the SLC was not that intense compared with the susceptible PM region of the -NSDL weldment.

3.1.2.1. Examination of surfaces after agar gel removal. Fig. 8(a) and (b) display the surfaces of the +NSDL and – NSDL weldments, respectively,

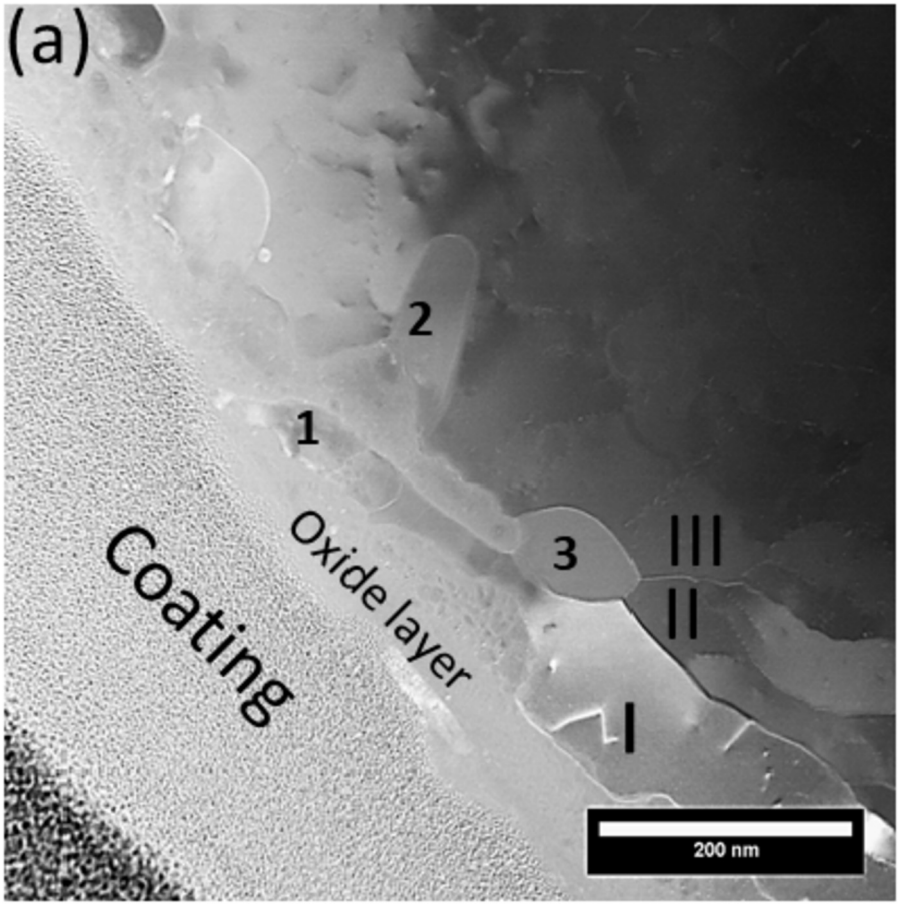

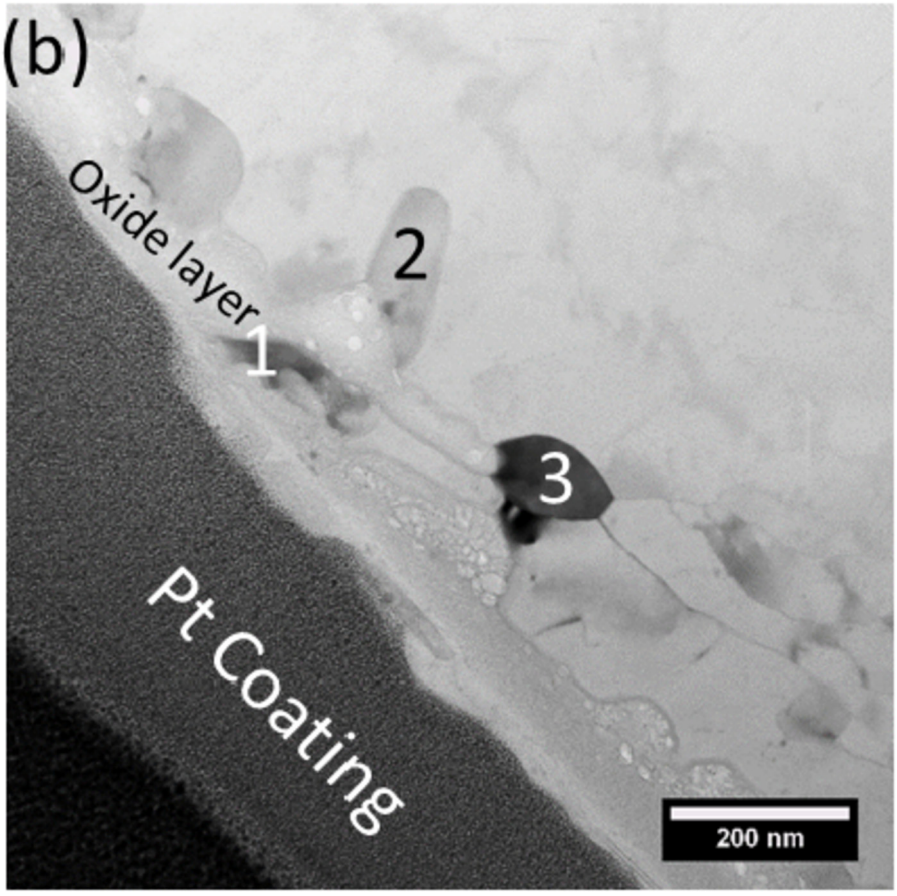

(caption on next page)

Fig. 4. (a) HAADF-STEM and (b) bright field TEM images of the cross-sectional view of the near-surface region of the AA2198-T851 alloy.

after the removal of the agar gel.

On the +NSDL weldment, the region with SLC sites is demarcated and labelled 1. Outside this region is an un-attacked region labelled 2 which encompasses the TMAZ, the weld and the PM side of the AS. Discontinuous dark features (demarcated by the rectangle in Fig. 8(a)) were present on the unpolished (+NSDL) weldment. These features (as indicated by the blue arrow in Fig. 6(a)) were more noble than the matrix in both the weld and TMAZ. EDS analysis (Fig. 9) of the region labelled x and y in Fig. 8(a) revealed that these features were composed of oxides of Fe and Si, indicating that they were lumps of coarse intermetallic particles rich in Fe and Si.

The Fe-Si rich intermetallic particles were concentrated on the flow arm (FA) region in the AS where materials from the RS of the weld had been dragged to. Generally, particles are the most easily conveyed material by the tool. Nonetheless, scanning electron microscopy analysis of the surface of the PM did not reveal any such lump of coarse intermetallic particles, except for magnesium-rich dark bands, as exemplified by the backscattered electron micrograph and the EDS maps previously shown in Fig. 3. This shows pronounced heterogeneities in the alloy microstructure; and this is corroborated by the fact that this sort of distribution is discontinuous, as it was not observed in the significant part of the weld seam.

On the -NSDL (polished) weldment in Fig. 8(b), there was a region of short-lived corrosion activities (labelled 3) on the RS of the weldment, as demarcated. In this region, corrosion initiated after about 2 h (as evident from the bubbles in Fig. 6(f) in the region labelled 3), but in the later hours of corrosion test, this region had transitioned to becoming a macro cathodic region with the significant generation of OH^-. This region was clearly repassivated, and this is evident, not only from the pink colouration observed in this region (Fig. 7(d)) but also from the surface appearance after removal of the agar gel. The appearance is obviously different from the appearance of the SLC site in region 1 as the surface was seemingly covered with a protective oxide layer.

In region 1, with a central pit and surrounding secondary evolving pits, as mentioned earlier, the appearance of the SLC pits was dark brown. On the corroded region of the +NSDL weldment (region 1 in Fig. 8(a)), the dark brown spots were not pronounced. This is because the lateral spread of attack was not as much as that of the polished weldment.

Furthermore, scanning electron micrographs of the corroded regions in the +NSDL weldment (Fig. 10(a)-(b)) and the –NSDL weldment (Fig. 10(c) and (d)) also clearly show that the corrosion morphologies in these two regions were different. This is supported by the optical images of the cross-sections across the SLC sites of the two weldments (Fig. 11). Presented in Fig. 12 is a schematic diagram explaining the differences in the SLC features of the PM sides of the polished and unpolished weldments.

Apart from the fact that the SLC pits were more dispersed on the +NSDL PM, the widths of the SLC pits were smaller, with deeper depths of penetration compared with those of the –NSDL PM. The attack was laterally spread in the –NSDL PM and the depth was shallow. A careful observation of the two surfaces appears to indicate that the pit mouths on the +NSDL PM were far smaller and were more covered with corrosion products, unlike those on the –NSDL PM which were relatively open. This may be a reason for the deeper pit depths observed on the +NSDL PM. In addition, the propagation pathways [37] were different: the polished side showed exfoliating layers as the corrosion propagated crystallographically; whereas exfoliating layers were not observed on the unpolished weldment. The corrosion morphologies were different because the near-surface deformed layer is of different metallurgical and chemical characteristics compared with the underlying bulk metal. This was mentioned in the introductory section of this work and shown in the TEM analysis presented earlier. However, a common feature observed from the corroded PM regions of the two weldments was the presence of redeposited Cu (as typified by the brighter spots (also indicated with arrows) in Fig. 10(c)). Presented in Fig. 13 are EDS maps obtained from a region in the vicinity of a severe localized corrosion pit on the +NSDL PM confirming the re-deposition of Cu. The framed region and the points (as shown by the arrows) clearly indicate that the bright features were indeed redeposited Cu. The redeposited Cu was from the non-faradaic release of Cu [38] that resulted primarily from the dissolution of active Cu-containing phases such as the T1 phase.

3.1.2.2. Potentiodynamic polarization behaviour of +NSDL and –NSDL surfaces. Presented in Fig. 14 are the potentiodynamic polarization curves of the polished and unpolished PM in acidified 3.5% NaCl solution. Two curves (labelled I and II) were presented for each case to show reproducibility. Acidified 3.5% NaCl solution was used because the differences between the two surfaces were pronounced in this solution compared with a less aggressive 3.5% NaCl solution.

A careful look at the curves shows that a slight pseudo-passive region was exhibited by the polished (-NSDL) PM prior to pronounced

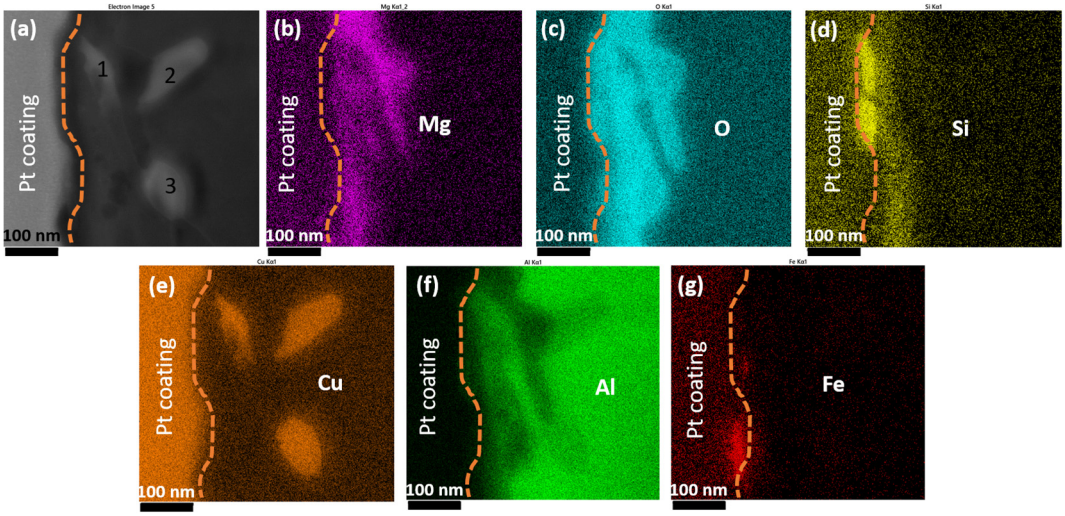

Fig. 5. EDS analyses of a region in Fig. 4 (a).

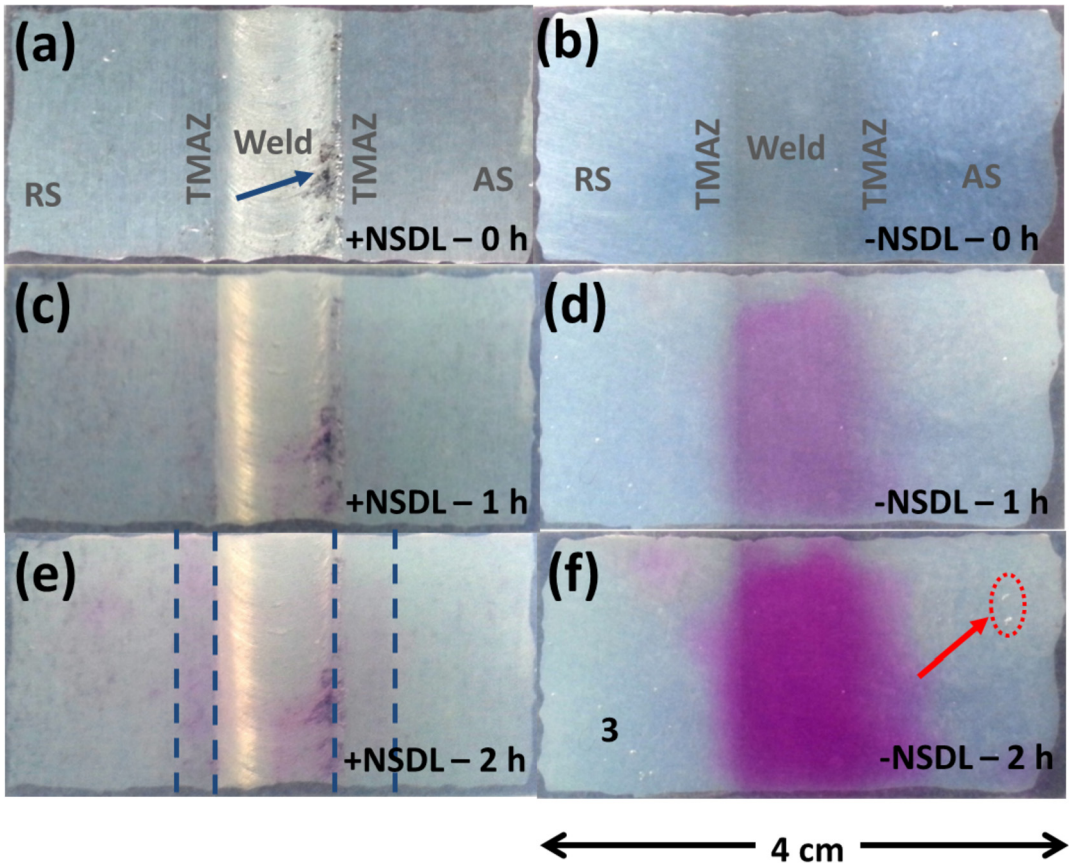

Fig. 6. Optical images of +NSDL (unpolished) and -NSDL (polished) friction stir weldments of the AA2198-T851 alloy in the early hours of agar gel corrosion visualization test.

dissolution. This sort of behaviour was not observed on the +NSDL PM indicating that the surface dissolved faster and more uniformly. Further, the presented polarization curves show that the presence of near-surface deformed layer led to an increase in current density values. This indicates an increase in the corrosion rate of the alloy surface when the near-surface deformed layer is not removed. However, the observed increase in current density is attributed to the activities across the entire examined surface and does not reflect the severity of the corrosion activities that occurred at each of the severe localized corrosion sites. The implication of this is that the number of pitting sites on the corroding PM of the -NSDL weldment was fewer compared with that of the +NSDL weldment. Also, the surface of the PM of the +NSDL weldment was more active and corroded more in a general form with pitting sites distributed across the entire surface owing to the presence

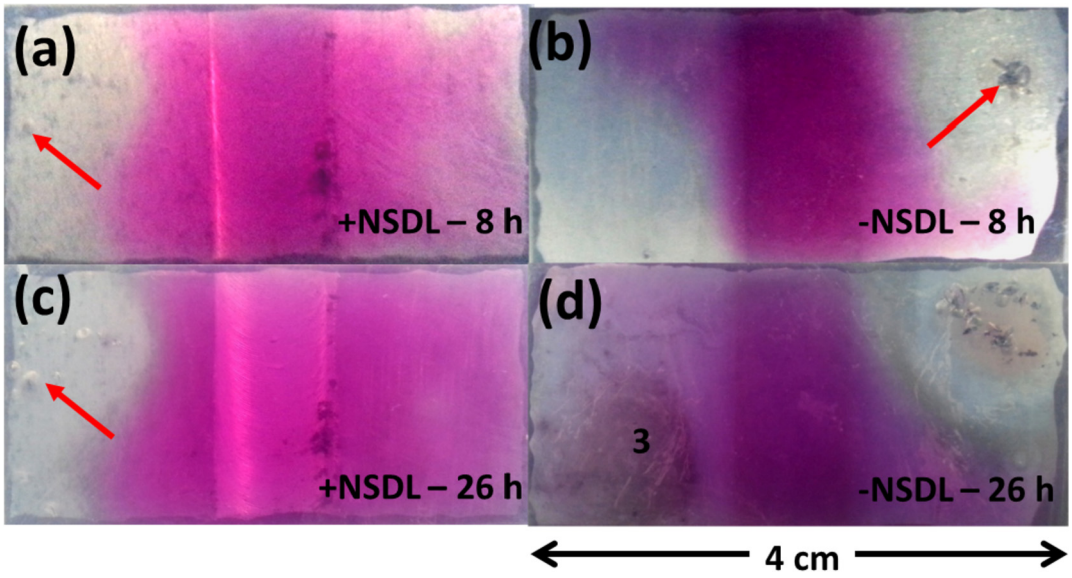

Fig. 7. ((a)–(d)) Optical images of +NSDL (unpolished) and -NSDL (polished) friction stir weldments of the AA2198-T851 alloy after ((a)–(b)) 8 h and ((c)–(d)) 26 h of agar gel corrosion visualization test.

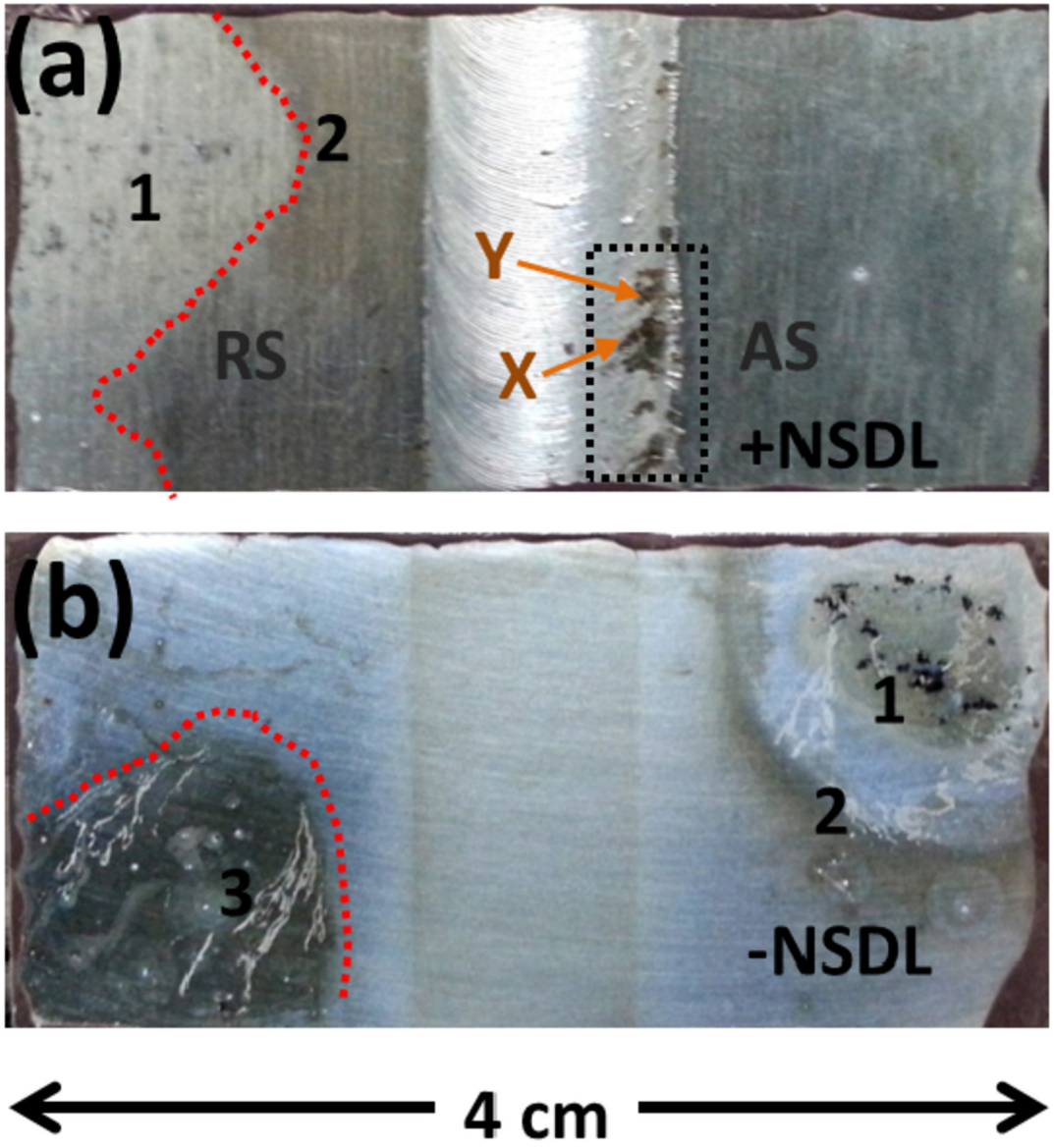

Fig. 8. Optical images of (a) unpolished and (b) polished weldments after the removal of the agar gel.

of higher Li and Mg contents (in bands). The Mg content in the manufacturing process induced NSDL is about ten times that of the underlying bulk, as revealed by EDS analysis. These analyses agree with the observed evolution of corrosion features during and after the agar gel corrosion visualization test.

3.2. Protection by anodizing

Given that the development of pronounced corrosion attack cannot be avoided in the PM side of the friction stir weldment of AA2198-T851 alloy irrespective of whether the surface is polished or not (as clearly depicted), protecting the weldment against corrosion is necessary. As mentioned earlier, anodizing is the most used method for the protection of Al alloys against corrosion. However, anodizing of weldments lead to pronounced formation of different thicknesses of anodic oxide layers on the individual zones of the weldment. Detailed investigation about these variations is rare to find in the literature. Thus, in this section, the corrosion behaviours of anodized and un-anodized weldment of the AA2198-T851 alloy have been compared, and efforts have also been made to shed more light on the factor (s) responsible for the differential oxide growth rates that occur during anodizing of the weldment. It must be mentioned that anodizing was not carried out on + NSDL weldment since surface pre-treatment must be carried out prior to anodizing. Anodizing surface pre-treatment methods remove manufacturing-process induced NSDL. In this study, polishing has been employed as a surface pre-treatment process since etching generates heterogeneities across weldments, and comparisons between anodized + NSDL and anosssized –NSDL samples were not made.

Displayed in Fig. 15 are potentiodynamic polarization curves of the anodized (unsealed) and un-anodized PM and SZ.

In the un-anodized condition, there was no pronounced difference in the current density values when the curve of the PM is compared with that of the SZ until about −0.6 V. From this potential, hydrogen bubble evolution began to interfere with the anodic polarization behaviour of the PM causing minute spikes which were not observed on the curve of the SZ. From about −0.3 V, pronounced spikes resulting from hydrogen bubble formation, coalescence and release were observed on the curve of the PM. These spikes were not pronounced on the curve of the SZ. However, a reduction in current density values was observed from −0.3 V to about 0.1 V for the curve of the SZ. This reduction was because the formed and coalesced bubbles were adhered to the surface causing a decrease of the actual surface area exposed to the

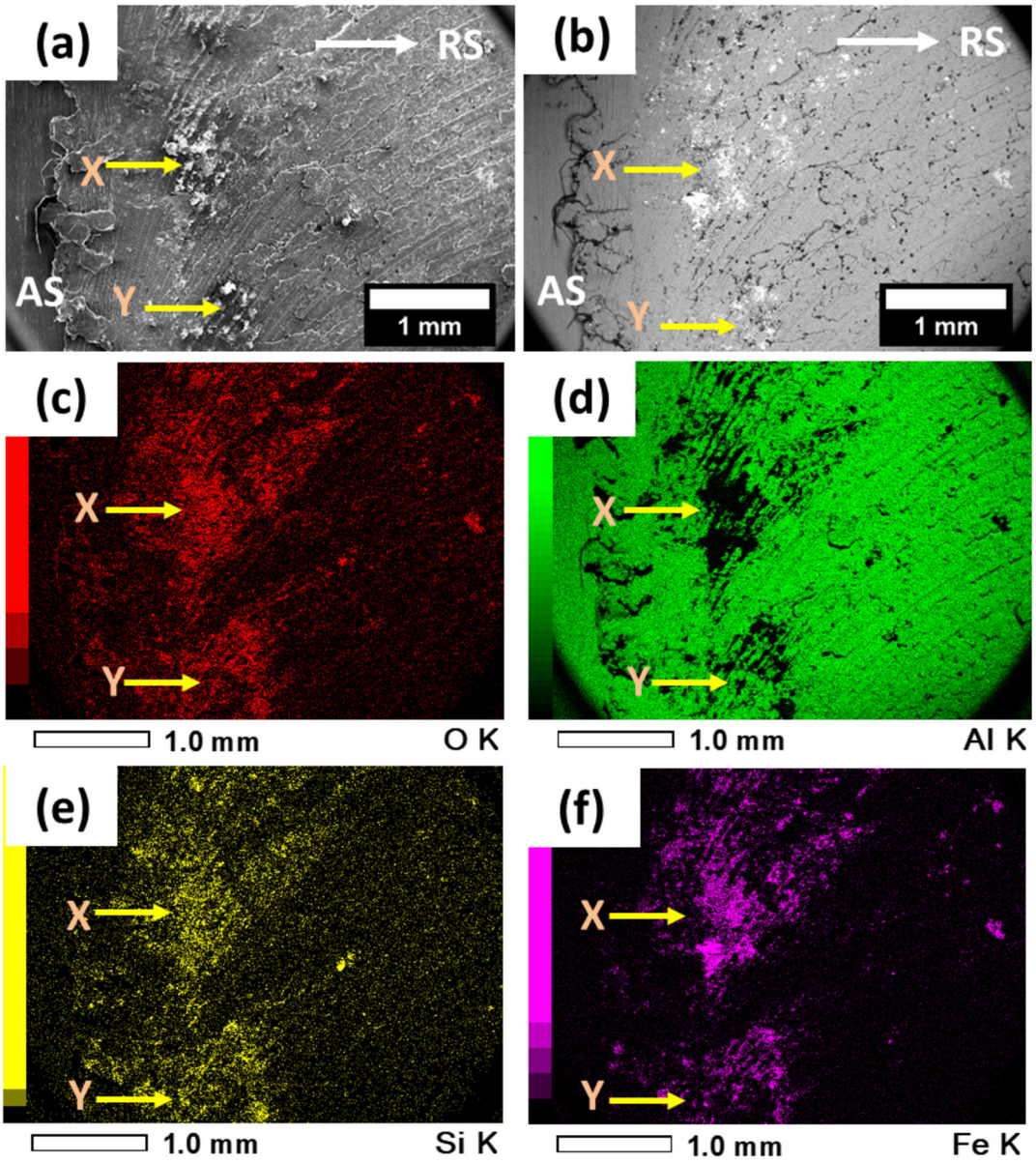

Fig. 9. ((a)–(b)) Scanning electron micrographs in secondary and backscattered electron modes, respectively, of the distinct feature observed in the AS of the friction stir weldment of the AA2198-T851 alloy. ((c)–(f)) EDS maps of the feature showing that they were composed of oxides of Fe- and Si-rich type coarse intermetallics.

electrolyte. The adherence in this region resulted from the formation of lesser hydrogen bubbles (compared with the volume produced on the PM in this region) which were not sufficient to force the detachment of large coalesced bubbles in quick succession. Because the release of large bubbles was minimal, less pronounced spikes were produced. In contrast, the volume of the one produced on the PM was much and the formation of adequate pressure to effect the detachment of large coalesced bubbles constantly occurred in quick successions. This phenomenon of having increased hydrogen evolution during anodic polarization is in contrast to electrochemical theory since hydrogen evolution is a cathodic process. Thus, it is often referred to as the negative difference effect (NDE), and it is commonly observed on Al and Mg alloys [38]. However, the deduction from this is that the PM was more susceptible to severe localized corrosion (associated with the evolution of H_2 bubbles), and this was why the volume of hydrogen bubbles produced during the polarization process was more on the PM compared with the SZ which was less susceptible.

Anodizing did not cause a reversal in corrosion susceptibility tendencies of the weld zones nor did it result in a uniform corrosion rate across the surface of the weldment. In fact, the corrosion rate of the PM in the anodic arm (of the potentiodynamic polarization curve of the anodized PM) was distinctly more than that of the SZ. However, anodizing significantly improved the corrosion resistance of the SZ and PM as expected. This was evident from the significant decrease in current density values (in the range of 2 decades for the PM and more than 3 decades for the SZ) and from the increase in corrosion potential from −0.66 V to −0.60 V vs Ag/AgCl. Actually, improvement in corrosion resistance due to anodizing is not a surprise. The main issue is the varying oxide growth rates that occur on different zones of weldments during anodizing. In a bid to solve this problem, understanding the mechanism and factors associated with the phenomenon is important.

Presented in Fig. 16 are the constant-voltage anodizing curves (Fig. 16(a)) and potentiodynamic anodizing curves (Fig. 16(b)) for the PM and weldment showing that welding affects the oxide growth rate on the AA2198-T851 alloy during anodizing. The constant-voltage curves show that prior to the onset of steady-state anodizing, the rate of current density increase was more for the weldment.

Further, at the start of steady-state anodizing, the current density

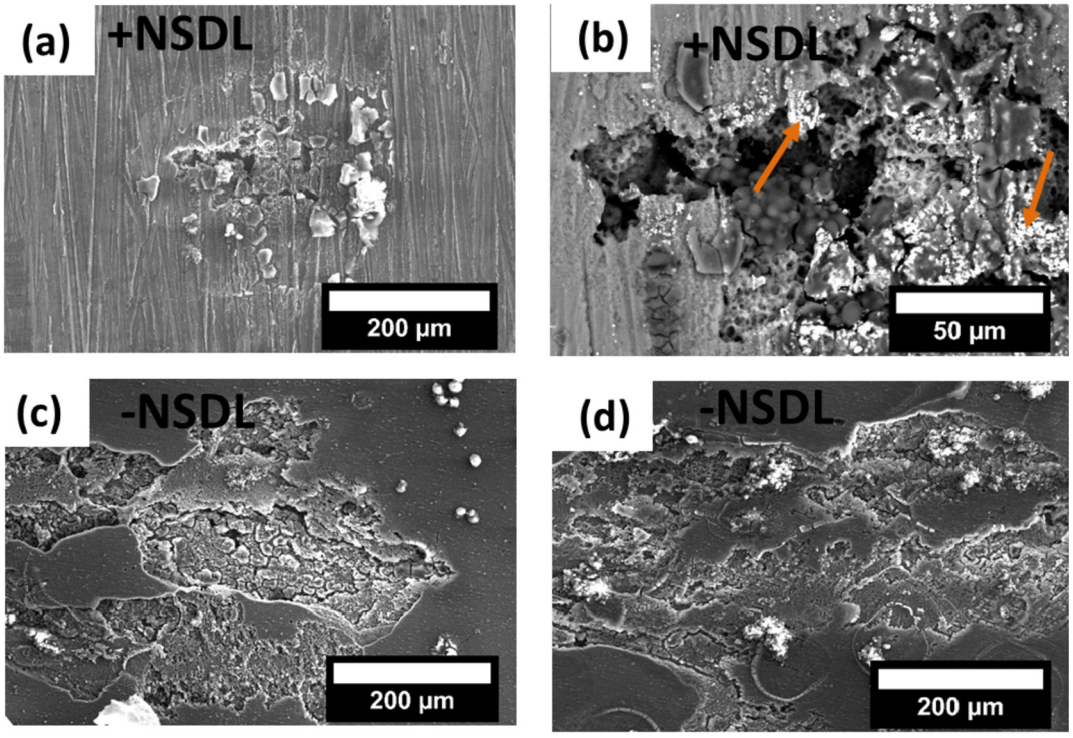

Fig. 10. ((a)–(b)) Scanning electron micrographs of the susceptible PM region in the +NSDL weldment of the AA2198-T851 alloy. ((c)–(d)) Scanning electron micrographs of the susceptible PM region in the - NSDL weldment of the AA2198-T851alloy.

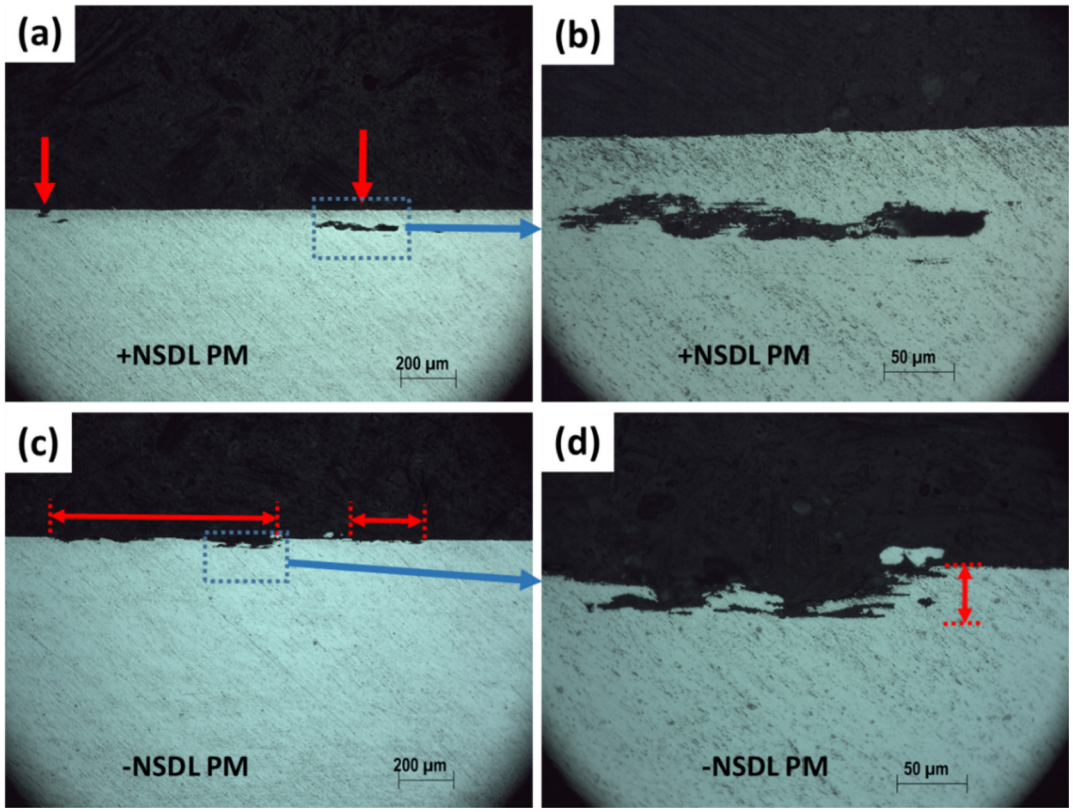

Fig. 11. Optical micrographs showing the cross-sectional views of the severe localized corrosion regions of the ((a)–(b)) +NSDL and ((c)–(d)) –NSDL weldments.

was higher (at about 0.060 A/cm^2) for the weldment but gradually reduced to values in the range of 0.056 A/cm^2 which was close to that of the PM in the range of 0.055 A/cm^2. This indicates that the overall charge (using the sum of current density x time) was more for the weldment compared with the PM. Consequently, the porous oxide thickness formed on the weldment will be higher.

Furthermore, at the early stage of the potentiodynamic anodizing, initial plateaux associated with the non-uniform film growth and

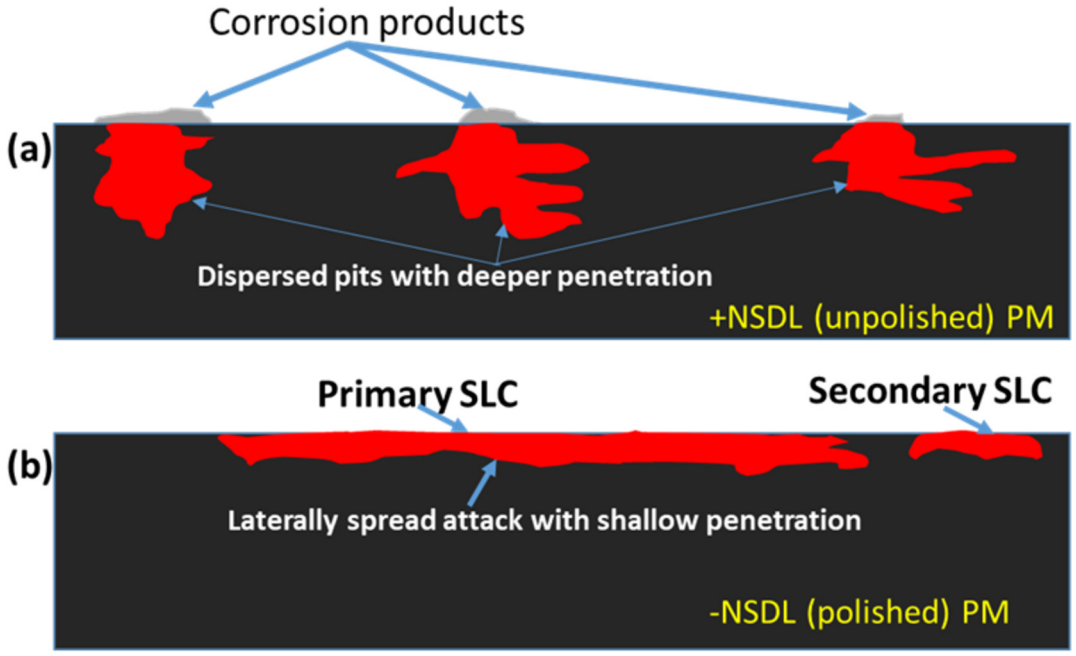

Fig. 12. Schematic diagram illustrating the differences in severe localized corrosion mechanisms between the +NSDL and –NSDL weldments.

development of the barrier layer [39] were observed between 0 and 0.5 V. Following this stage, current density increases with increasing potential values were observed up to about 1 V. This second stage is associated with the development of incipient pores [40]. Subsequently, the current density increased exponentially with potential, and this stage is associated with the usual porous anodic film growth [39]. From

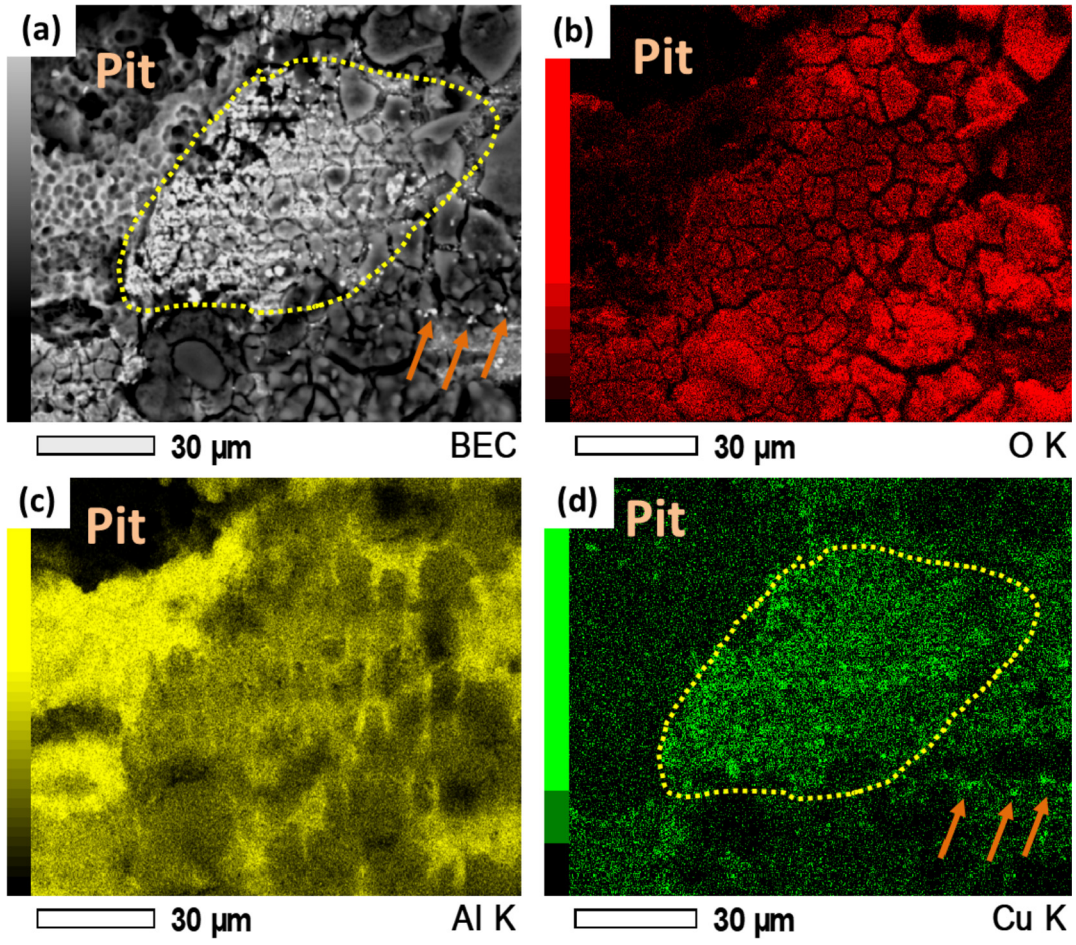

Fig. 13. EDS analysis of a severe localized corrosion pit region on the +NSDL PM showing Cu re-deposition.

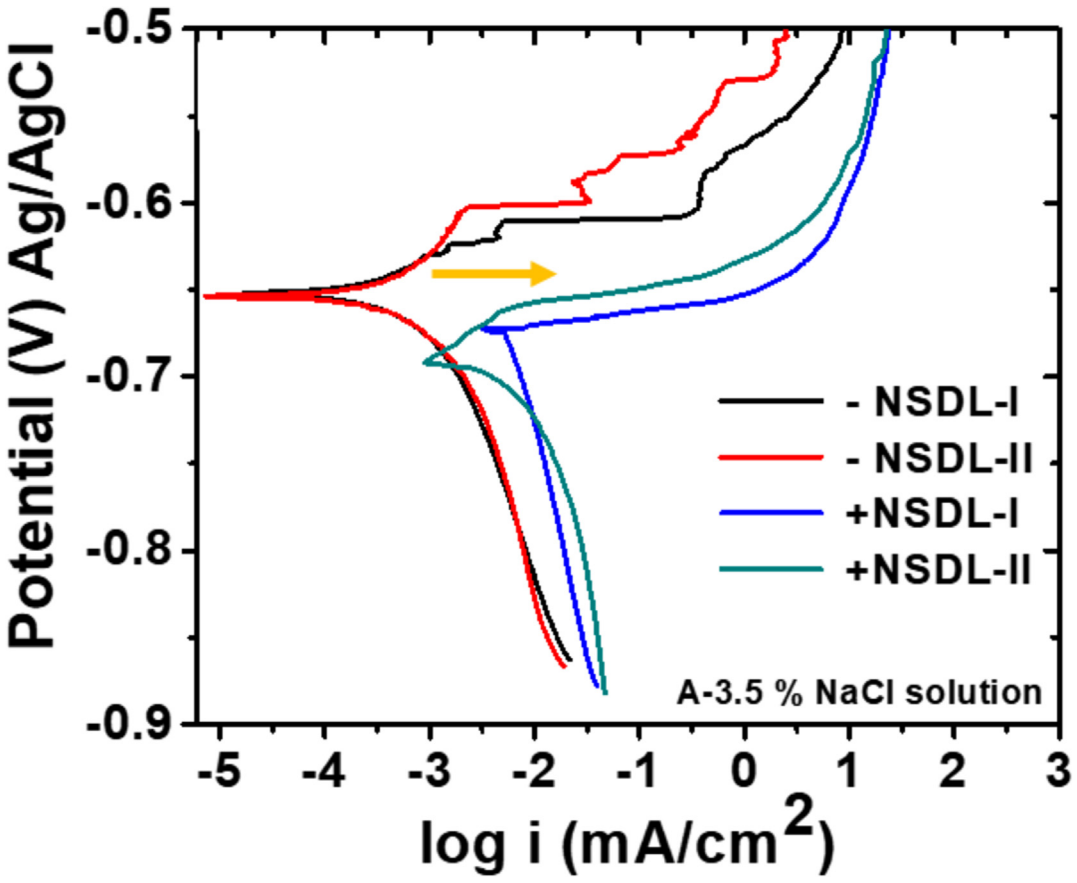

Fig. 14. Potentiodynamic polarization curves of the +NSDL and -NSDL samples in A-3.5% NaCl solution.

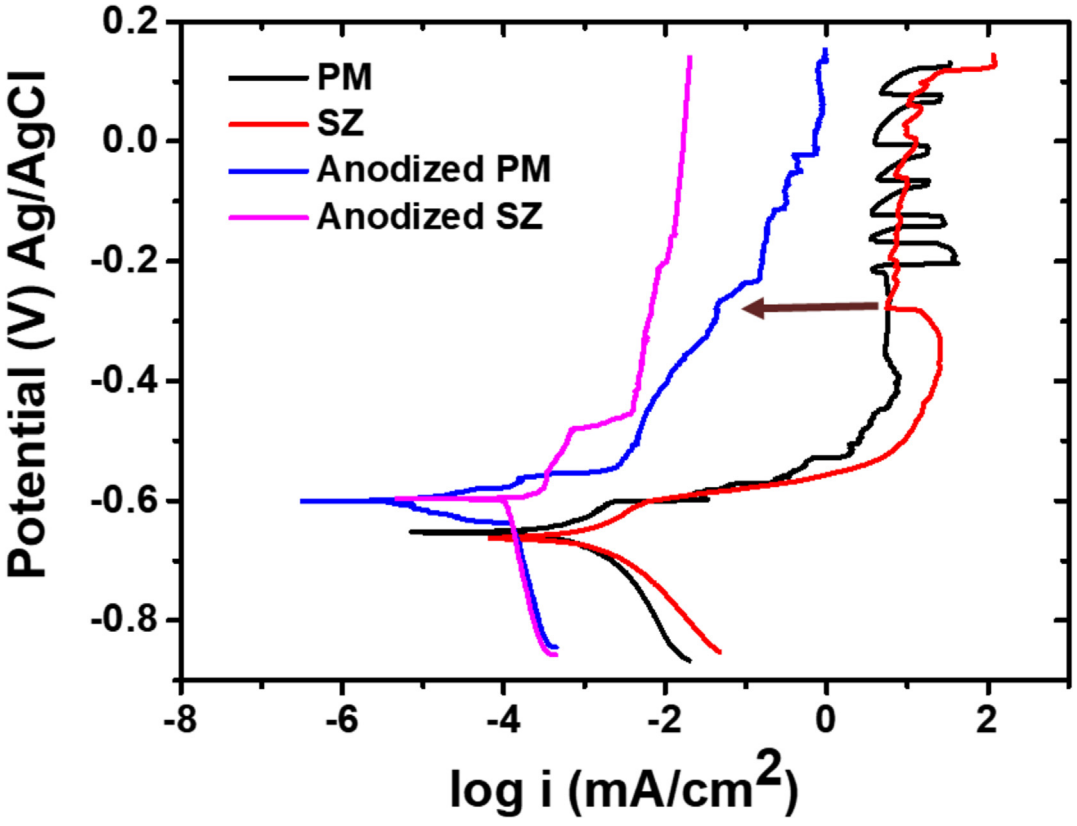

Fig. 15. Potentiodynamic polarization curves of anodized and un-anodized PM and SZ regions in A-3.5% NaCl solution.

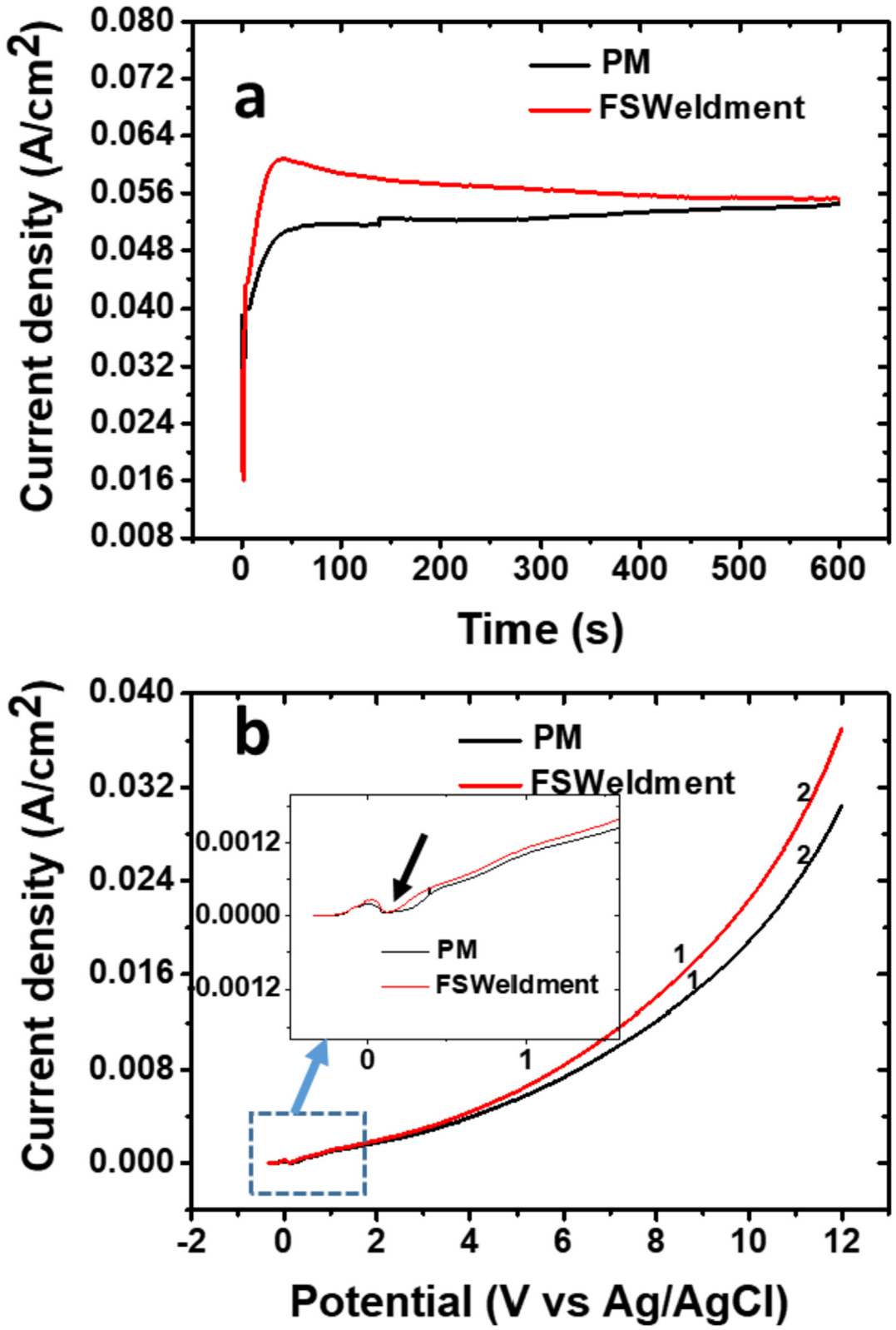

Fig. 16. (a) Potentiostatic anodization curves of the PM and friction stir weldment of the AA2198-T851 alloy. (b) Potentiodynamic anodization curves of the PM and friction stir weldment of the AA2198-T851 alloy.

the inset in Fig. 16(b), the early stage behaviour associated with the barrier layer growth and development was shorter for the weldment compared with the PM. This probably means that the required maximum barrier layer thicknesses prior to the formation of pores for the HAZ, TMAZ and SZ are lower compared with that for the PM. This resulted in the faster development of pores on the weldment. This speedy formation was due to the increased oxidation on the SZ in particular. After this stage (from about 0.5 V to 1 V), the behaviour of both, the PM and the weldment, were about the same and the slopes were largely similar. From approximately 1 V, the difference in the

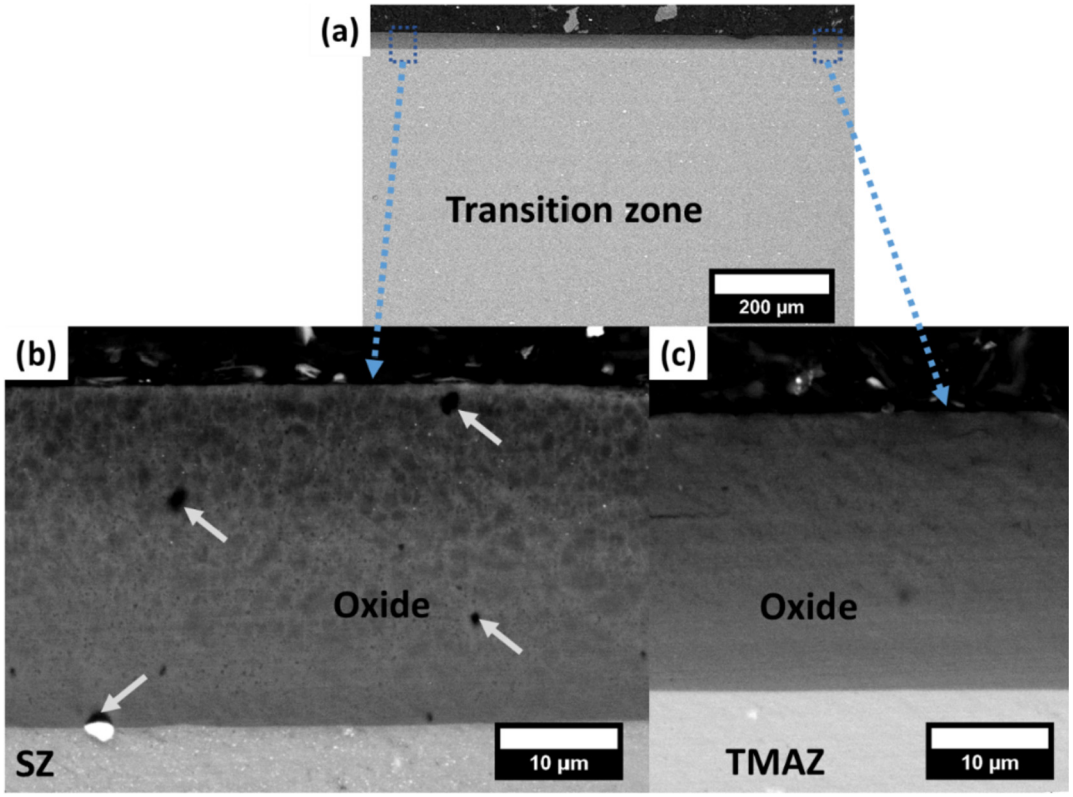

Fig. 17. Cross-sectional micrographs of the SZ/TMAZ/HAZ transition region of the AA2198-T851 friction stir weldment after potentiostatic anodizing.

anodizing responses of the two became apparent. Calculated slopes from tangents drawn across points 1 and 2, as indicated on the curves, yielded values of 3.90 mA/cm^2/V and 7.90 mA/cm^2/V for the weldment, and 3.32 mA/cm^2/V and 5.47 mA/cm^2/V for the PM, respectively. Thus, the rate of porous oxide layer formation on the weldment was more than that on the PM, especially as 12 V was approached.

For further clarification, SEM images of the cross-sections of anodized samples were examined. Presented in Fig. 17 are the SEM images of the transition region between the SZ, TMAZ and HAZ. The thickness range of porous oxide layer on the SZ (measured from Fig. 17(b)) was 29.0 ± 0.15 μm whilst that on the TMAZ/HAZ (from Fig. 17(c)) was 23.9 ± 0.13 μm. Presented in Fig. 18 are the SEM images of the mid part of the SZ (Fig. 18(a)-(b)) and that of the PM (Fig. 18(c)-(d)). The measured thickness range for the porous oxide layer on the PM was 21.0 ± 0.25 μm. Thus, from PM to TMAZ/HAZ and to SZ, the range of thicknesses increased.

Evidently, the increased oxidation rates on the SZ and TMAZ/HAZ regions were the reasons for the overall higher current density observed at the steady state during potentiostatic anodizing and higher increasing rates of current density during potentiodynamic anodizing. These oxide thickness variations appear to agree with the microhardness profile across the friction stir weldment. Presented in Fig. 19 is the microhardness profile of the advancing side of the friction stir weldment which shows that the PM had the highest hardness values, in the range of 190 HV/0.3, whilst the HAZ showed decreasing hardness values from the PM to the HAZ/TMAZ boundary, with a hardness value of about 103 HV/0.3. The hardness values recorded in the SZ were in the range of 110 HV/0.3.

The variation in the hardness values was due to differences in the volume fractions of the T1 particles across the different zones. The region with the highest volume fraction of T1 phase exhibited the highest hardness, whilst the region with the lowest volume fraction exhibited the lowest hardness. Thus, there appears to be an inverse relationship between hardness and the degree of oxidation or consumption of the base metal in the individual weld zones. Undoubtedly, hardness and state of stress in Al alloys affect structural features of porous anodic oxide layers formed on Al alloys. As an example, Stepniowski et al. [41] showed that cold deformation of an AA1050 significantly altered pore density and interpore distance and that even at a 20% degree of prior deformation anodizing was difficult at a potential of 20 V. The alloy corroded instead of forming a porous anodic oxide layer. But then, the differences in oxide layer thicknesses do not correspond with the differences in hardness values. The hardness profile shows that there are regions just outside the SZ with lower or equal hardness values (at the HAZ/TMAZ as indicated by the shaded portion in Fig. 19), and these regions formed thinner oxide layers compared with the SZ. This is also evident from the scanning electron micrograph of the transition region shown in Fig. 17. Further, in previous work by Ref. [22], the SZ with the least hardness was reported to have formed the lowest porous oxide thickness compared with the other zones, such as the PM side of the AA5083-O alloy. Thus, other metallurgical factors such as grain size, distinct zonal precipitation and solid solution composition, in addition to hardness, may be responsible for the differential oxidation of the weld zones. At least, the grain sizes in the SZ is ultrafine and significantly different from that of the HAZ, PM and the TMAZ outside the tool domain. In this case, the closest relationship happens to be the volume fraction of the T1 particles which is highest in the PM but decreases towards the SZ where peak temperature values were attained during the welding process. Thus, in order of T1 density, the PM > HAZ > TMAZ > SZ and this is exactly inversely proportional to the variation in porous oxide thicknesses in these zones. Accordingly, the Li content in solid solution also increased in the same order. This is because Li is a major component of the T1 phase, and a decrease in the volume fraction of the T1 particles will correspond to an increase in the Li content in solid solution. Thus, it is proposed here that the higher the Li content in solid solution, the higher the oxidation rate of the region during anodizing. This agrees well with the variations in oxide layer thicknesses as the Li content in solid solution increased continuously

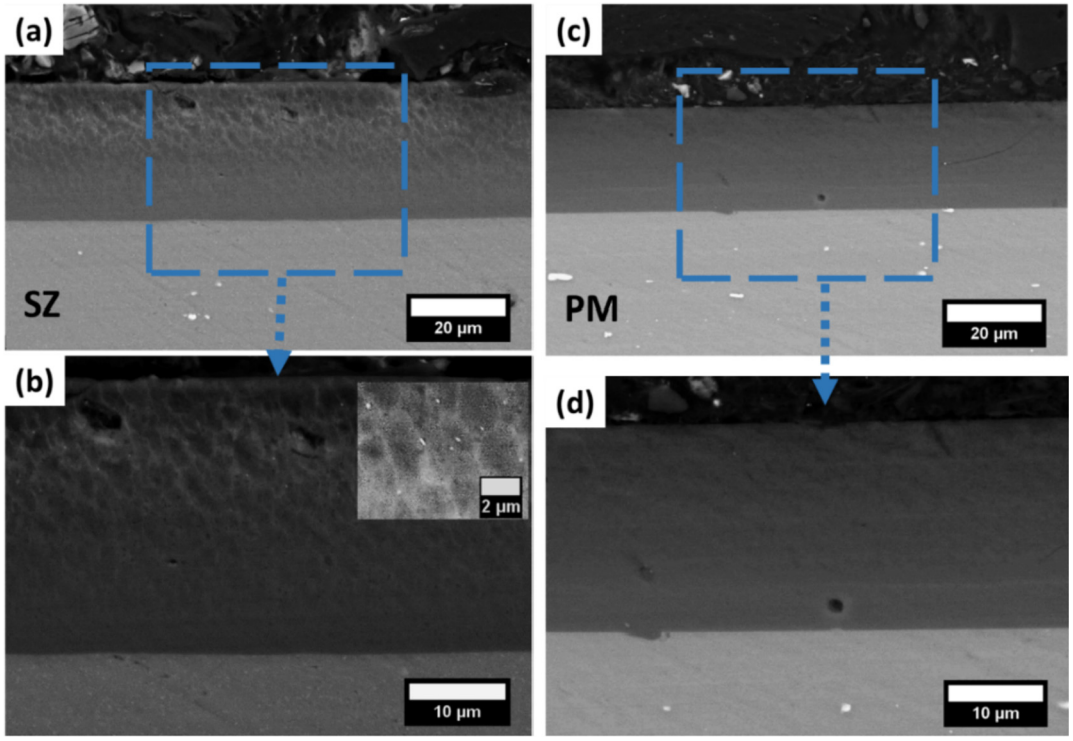

Fig. 18. Cross-sectional micrographs of the ((a)–(b)) SZ and ((c)–(d)) PM regions of the AA2198-T851 friction stir weldment after potentiostatic anodizing.

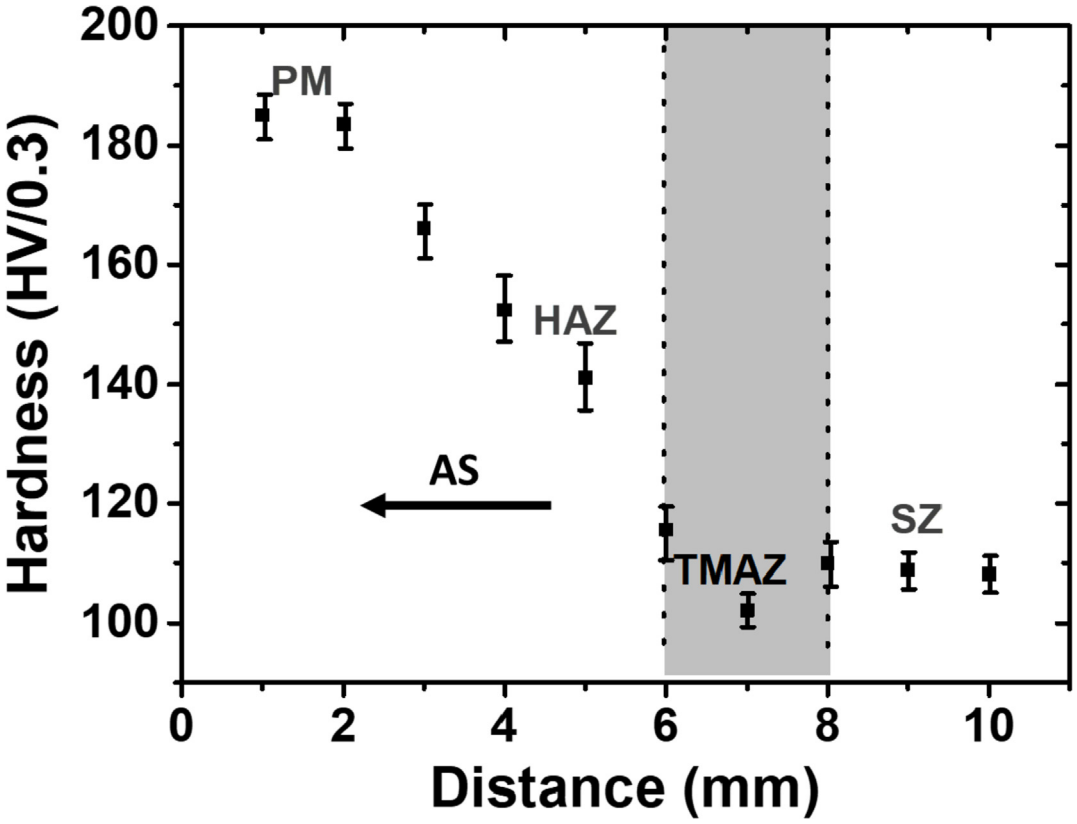

Fig. 19. Vickers microhardness profile obtained from the PM side of the weldment to the weld centre region for the unanodized surface of the AA2198-T851 friction stir weldment.

from the PM to the SZ owing to the decrease in T1 concentration from the PM to the SZ.

Another point to note is that other anodic oxide layer features were observed from the cross-sectional examination. These features were the typical particle induced defects (when porous anodic oxide layer is formed on an Al alloy) caused by the differential oxidation rates of the particles compared with that of the matrix, as indicated by the arrows in Fig. 17(b); and incorporated fine particles, as shown in the inset in Fig. 18(b). The first features were found in all the zones of the weld since they all contained the Cu-Fe rich coarse intermetallic particles. The differential oxidation of these particles resulted in the formation of cracks, voids and tortuous pore morphology in the porous oxide layer which are rare features in the porous oxide layers on a pure Al [42]. However, the second features were only found in the SZ. The incorporated particles are the suspected T_B particles earlier shown in Fig. 2(c). Evidently, these particles do not get oxidized under the electric field and are incorporated into the oxide as the matrix is consumed. Nonetheless, it is highly unlikely that the presence of these particles affected the preferential oxide formation rate on the SZ, since their effect would most likely be the retardation of the oxide growth rate and not the opposite. Secondly, the oxide layer on the HAZ/TMAZ were thicker and these phase was not in abundance in these regions. On the other hand, it is important to note that the incorporation of suspected T_B particles in the oxide layer may affect the behaviour of the oxide layer during further processing, such as sealing.

Lastly, in addition to the variations in oxide layer thicknesses across the weld zones, microhardness values obtained across the anodized surface of the weldment (Fig. 20) showed a reversed microhardness profile with respect to the microhardness profile of the un-anodized surface of the weldment (previously shown in Fig. 19).

This indicates that the pore morphologies are different from zone to zone, and the porous oxide formed on the SZ may have the shortest inter-pore distance and/or thickest cell walls compared with that formed on the other zones. Also, the porous oxide layer formed on the SZ was the least ductile. This deduction is from the fact that pronounced cracks were observed at the edges of the indent made during microhardness measurements. Little or no cracks were observed on the oxide layer on the PM indicating that it was the most ductile oxide layer region on the anodized surface of the weldment. However, further morphological characterization of the porous oxides formed on the different zones is necessary, and this is proposed for future work.

4. Conclusions

The corrosion and anodizing behaviour of the AA2198-T851 alloy friction stir weldment have been studied, and the following conclusions are drawn.

1. The corrosion behaviour of an unpolished weldment is different from that of the polished weldment due to the presence of manufacturing-process induced near-surface deformed layer in the former. However, in both cases, the PM sides were the most susceptible regions in the friction stir weldment of the AA2198-T851 alloy, because of the high density of T1 particles in the PM.
2. Severe localized corrosion sites were more evenly spread on the susceptible region in the unpolished weldment compared with the polished one. In addition, the attack penetrated more on the unpolished PM because of the smaller pit mouth and coverage by corrosion products; whereas, for the polished, the attack spread laterally and appeared to be more intense.
3. Anodizing generally increased the corrosion resistance of the friction stir weldment. However, sulfuric acid anodization resulted in the formation of different porous oxide layer thicknesses across the weld zones. The weldment oxidized at a higher rate during anodizing due to the increased rate of oxide layer formation on the TMAZ/HAZ and the SZ compared with the PM. The SZ exhibited the

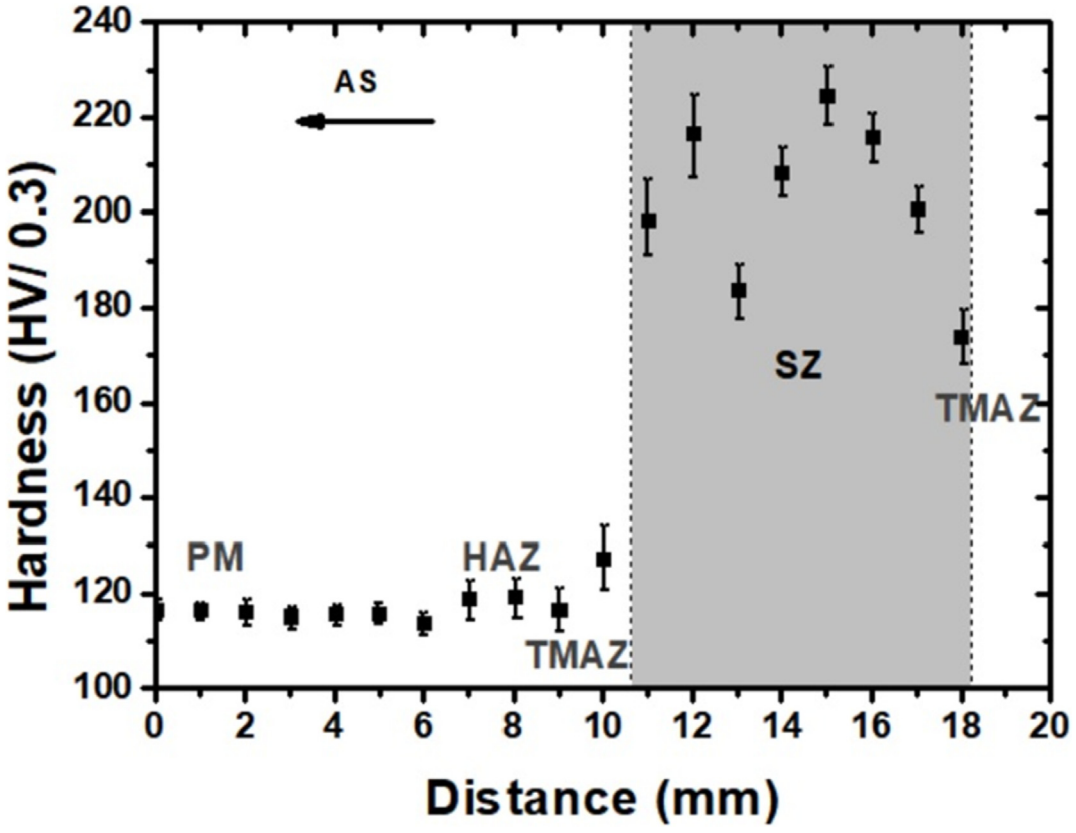

Fig. 20. Vickers microhardness profile obtained from the PM side to the SZ for the anodized surface of the AA2198-T851 friction stir weldment.

highest oxide growth rates in all the weld zones.

4. There appeared to be a strong inverse relationship between hardness and degree of oxide layer formation across the weld zones. However, there were regions of lower hardness values with lesser degree of oxidation compared with the SZ. Thus, a combination of factors may be responsible for the variations in oxide layer thicknesses across the weld zones. Nonetheless, the Li content in solid solution has been proposed to be a significant reason for the differences in oxide layer thicknesses observed.
5. Microhardness profile across the anodized surface of the weldment has an inverse relationship with the microhardness profile across the un-anodized surface of the weldment. The lowest hardness value on the un-anodized surface of the weldment was recorded in the SZ, whereas the highest value was recorded in the SZ for the anodized surface.

Data availability

The raw/processed data required to reproduce these findings cannot be shared at this time as the data also forms part of an ongoing study.

Acknowledgement

The authors are grateful to FAPESP for the sponsorship of Dr Uyime Donatus Postdoctoral fellowship (Process2017/03095-3) and for financial support for this research (Process 2013/13235-6).

References

[1] P.L. Threadgill, A.J. Leonard, H.R. Shercliff, P.J. Withers, Friction stir welding of aluminium alloys, Int. Mater. Rev. 54 (2009) 49–93, https://doi.org/10.1179/174328009X411136.

[2] V. Proton, J. Alexis, E. Andrieu, C. Blanc, J. Delfosse, L. Lacroix, G. Odemer, Influence of post-welding heat treatment on the corrosion behavior of a 2050-T3 aluminum-copper-lithium alloy friction stir welding joint, J. Electrochem. Soc. 158 (2011) C139–C147, https://doi.org/10.1149/1.3562206.

[3] V. Proton, J. Alexis, E. Andrieu, J. Delfosse, A. Deschamps, F. De Geuser, M.C. Lafont, C. Blanc, The influence of artificial ageing on the corrosion behaviour of a 2050 aluminium-copper-lithium alloy, Corrosion Sci. 80 (2014) 494–502, https://doi.org/10.1016/j.corsci.2013.11.060.

[4] M. Jariyaboon, A.J. Davenport, R. Ambat, B.J. Connolly, S.W. Williams, D.A. Price, The effect of welding parameters on the corrosion behaviour of friction stir welded AA2024-T351, Corrosion Sci. 49 (2007) 877–909.

[5] M. Esmaily, N. Mortazavi, W. Osikowicz, H. Hindsefelt, J.E. Svensson, M. Halvarsson, G.E. Thompson, L.G. Johansson, Corrosion behaviour of friction stir-welded AA6005-T6 using a bobbin tool, Eval. Progr. Plann. 111 (2016) 98–109, https://doi.org/10.1016/j.corsci.2016.04.046.

[6] M. Esmaily, Z. Mortazavi, C. Osikowicz, C.E. Hindsefelt, Svensson, M. Halvarsson, B.E. Thompson, A.G. Johanssona, Influence of multi-pass friction stir processing on the corrosion behavior of an Al-Mg-SiAlloy, J. Electrochem. Soc. 163 (2016) 124–130, https://doi.org/10.1149/2.1091603jes.

[7] C.P. de Abreu, I. Costa, H.G. de Melo, N. Pébère, B. Tribollet, V. Vivier, Multiscale electrochemical study of welded Al alloys joined by friction stir welding, J. Electrochem. Soc. 164 (2017) C735–C746, https://doi.org/10.1149/2.0391713jes.

[8] W. Xu, J. Liu, Microstructure and pitting corrosion of friction stir welded joints in 2219-O aluminum alloy thick plate, Corrosion Sci. 51 (2009) 2743–2751, https://doi.org/10.1016/j.corsci.2009.07.004.

[9] X. Zhang, B. Liu, X. Zhou, J. Wang, T. Hashimoto, C. Luo, Z. Sun, Z. Tang, F. Lu, Laser welding introduced segregation and its influence on the corrosion behaviour of Al-Cu-Li alloy, Corrosion Sci. 135 (2018) 177–191, https://doi.org/10.1016/j.corsci.2018.02.044.

[10] E. Bousquet, A. Poulon-Quintin, M. Puiggali, O. Devos, M. Touzet, Relationship between microstructure, microhardness and corrosion sensitivity of an AA 2024-T3 friction stir welded joint, Corrosion Sci. 53 (2011) 3026–3034, https://doi.org/10.1016/j.corsci.2011.05.049.

[11] X. Zhang, B. Liu, X. Zhou, J. Wang, C. Luo, Z. Sun, Z. Tang, F. Lu, J.W. Xinxin Zhang, Liu Bing, Z.T. Xiaorong Zhou, F.L. Chen Luo, Sun Zhihua, X. Zhang, B. Liu, X. Zhou, J. Wang, C. Luo, Z. Sun, Z. Tang, F. Lu, Corrosion behavior of friction stir welded 2A97 Al-Cu-Li alloy, Corrosion 9312 (2017) 2418, https://doi.org/10.5006/2418.

[12] J. Kang, R. Fu, G. Luan, C. Dong, M. He, In-situ investigation on the pitting corrosion behavior of friction stir welded joint of AA2024-T3 aluminium alloy, Corrosion Sci. 52 (2010) 620–626, https://doi.org/10.1016/j.corsci.2009.10.027.

[13] W. Xu, J. Liu, H. Zhu, Pitting corrosion of friction stir welded aluminum alloy thick plate in alkaline chloride solution, Electrochim. Acta 55 (2010) 2918–2923, https://doi.org/10.1016/j.electacta.2009.12.083.

[14] J.C.B. Bertoncello, S.M. Manhabosco, L.F.P. Dick, Corrosion study of the friction stir lap joint of AA7050-T76511 on AA2024-T3 using the scanning vibrating electrode technique, Corrosion Sci. 94 (2015) 359–367, https://doi.org/10.1016/j.corsci.2015.02.029.

[15] A. Cassell, G.E. Thompson, X. Zhou, A. Afseth, H. Dunlop, M.A. Kulas, L. Peguet, G. Scamans, Microstructure and corrosion behaviour of low copper 7xxx aluminium alloy, Surf. Interface Anal. 45 (2013) 1604–1609, https://doi.org/10.1002/sia.5226.

[16] Y. Liu, A. Laurino, T. Hashimoto, X. Zhou, P. Skeldon, G.E. Thompson, G.M. Scamans, C. Blanc, W.M. Rainforth, M.F. Frolish, Corrosion behaviour of mechanically polished AA7075-T6 aluminium alloy, Surf. Interface Anal. 42 (2010) 185–188, https://doi.org/10.1002/sia.3136.

[17] S.-S. Wang, G.S. Frankel, J.-T. Jiang, J.-F. Chen, S.-L. Dai, L. Zhen, Mechanism of localized breakdown of 7000 series aluminum alloys, J. Electrochem. Soc. 160 (2013) C493–C502, https://doi.org/10.1149/2.080310jes.

[18] B. Liu, X. Zhang, X. Zhou, T. Hashimoto, J. Wang, The corrosion behaviour of machined AA7150-T651 aluminium alloy, Corrosion Sci. 126 (2017) 265–271, https://doi.org/10.1016/j.corsci.2017.07.008.

[19] G.M. Scamans, M.F. Frolish, W.M. Rainforth, Z. Zhou, Y. Liu, X. Zhouc, G.E. Thompsonc, The ubiquitous beilby layer on aluminium surfaces, Surf. Interface Anal. 42 (2010) 175–179, https://doi.org/10.1002/sia.3204.

[20] V. Proton, J. Alexis, E. Andrieu, J. Delfosse, M.-C. Lafont, C. Blanc, Characterisation and understanding of the corrosion behaviour of the nugget in a 2050 aluminium alloy Friction Stir Welding joint, Corrosion Sci. 73 (2013) 130–142, https://doi.org/10.1016/j.corsci.2013.04.001.

[21] R.S. Mishra, Z.Y. Ma, Friction stir welding and processing, Mater. Sci. Eng. R Rep. 50 (2005) 1–78, https://doi.org/10.1016/j.mser.2005.07.001.

[22] U. Donatus, G.E. Thompson, X. Zhou, Anodizing behavior of friction stir welded dissimilar aluminum alloys, J. Electrochem. Soc. 162 (2015) C657–C665, https://doi.org/10.1149/2.0651512jes.

[23] U. Donatus, G.E. Thompson, X. Zhou, Effect of prior sputter deposition of pure aluminium on the corrosion behaviour of anodized friction stir weld of dissimilar aluminium alloys, SMM 123 (2016) 126–129, https://doi.org/10.1016/j.scriptamat.2016.06.015.

[24] U. Donatus, G.E. Thompson, X. Zhou, J. Wang, A. Cassell, K. Beamish, Corrosion susceptibility of dissimilar friction stir welds of AA5083 and AA6082 alloys, Mater. Char. 107 (2015) 85–97, https://doi.org/10.1016/j.matchar.2015.07.002.

[25] M.X. Milagre, N.V. Mogili, U. Donatus, R.A.R. Giorjão, M. Terada, J.V.S. Araujo, C.S.C. Machado, I. Costa, On the microstructure characterization of the AA2098-T351 alloy welded by FSW, Mater. Char. 140 (2018) 233–246, https://doi.org/10.1016/j.matchar.2018.04.015.

[26] S.Y. Duan, C.L. Wu, Z. Gao, L.M. Cha, T.W. Fan, J.H. Chen, Interfacial structure evolution of the growing composite precipitates in Al-Cu-Li alloys, Acta Mater. 129 (2017) 352–360, https://doi.org/10.1016/j.actamat.2017.03.018.

[27] U. Donatus, B.V.G. de Viveiros, M.C. de Alencar, R.O. Ferreira, M.X. Milagre, I. Costa, Correlation between corrosion resistance, anodic hydrogen evolution and microhardness in friction stir weldment of AA2198 alloy, Mater. Char. 144 (2018) 99–112, https://doi.org/10.1016/j.matchar.2018.07.004.

[28] J.V. de Sousa Araujo, U. Donatus, F.M. Queiroz, M. Terada, M.X. Milagre, M.C. de Alencar, I. Costa, On the severe localized corrosion susceptibility of the AA2198-T851 alloy, Corrosion Sci. 133 (2018) 132–140, https://doi.org/10.1016/j.corsci.2018.01.028.

[29] U. Donatus, M. Terada, C.R. Ospina, F.M. Queiroz, A. Fatima Santos Bugarin, I. Costa, On the AA2198-T851 alloy microstructure and its correlation with localized corrosion behaviour, Corrosion Sci. 131 (2018) 300–309, https://doi.org/10.1016/j.corsci.2017.12.001.

[30] P. Atz Dick, G.H. Knörnschild, L.F.P. Dick, Anodising and corrosion resistance of AA 7050 friction stir welds, Corrosion Sci. 114 (2017) 28–36 http://www.sciencedirect.com/science/article/pii/S0010938X16309957 , Accessed date: 7 November 2016.

[31] U. Donatus, G.E. Thompson, S. Morsch, I.-L. Tsai, Areas of concern in an anodised dissimilar friction stir weld of AA5083 and AA6082 aluminium alloys, Trans. Inst. Met. Finish. 94 (2016) 70–75, https://doi.org/10.1080/00202967.2016.1155880.

[32] D.L. Chen, M.C. Chaturvedi, Effects of welding and weld heat-affected zone simulation on the microstructure and mechanical behavior of a 2195 aluminum-lithium alloy, Metall. Mater. Trans. A Phys. Metall. Mater. Sci. 32 (2001) 2729–2741, https://doi.org/10.1007/s11661-001-1025-6.

[33] P.S. Chen, B.N. Bhat, Time-temperature-precipitation behavior in AI-Li alloy 2195, Tech. Rep. (2002), http://ntrs.nasa.gov/archive/nasa/casi.ntrs.nasa.gov/20020030744.pdf.

[34] F. De Geuser, B. Malard, A. Deschamps, Microstructure mapping of a friction stir welded AA2050 Al-Li-Cu in the T8 state, Philos. Mag. A 94 (2014) 1451–1462, https://doi.org/10.1080/14786435.2014.887862.

[35] R.W. Fonda, J.F. Bingert, Precipitation and grain refinement in a 2195 Al friction stir weld, Metall. Mater. Trans. A Phys. Metall. Mater. Sci. 37 (2006) 3593–3604, https://doi.org/10.1007/s11661-006-1054-2.

[36] J.C. Rao, E.J. Payton, C. Somsen, K. Neuking, G. Eggeler, A. Kostka, J.F. Dos Santos, Where does the lithium go? - a study of the precipitates in the stir zone of a friction stir weld in a Li-containing 2xxx series Al alloy, Adv. Eng. Mater. 12 (2010) 298–303, https://doi.org/10.1002/adem.200900284.

[37] U. Donatus, G.E. Thompson, J.A. Omotoyinbo, K.K. Alaneme, S. Aribo, O.G. Agbabiaka, Corrosion pathways in aluminium alloys, Trans. Nonferrous Metals Soc. China 27 (2017) 55–62, https://doi.org/10.1016/S1003-6326(17)60006-2.

[38] G.S. Frankel, S. Fajardo, B.M. Lynch, Introductory lecture on corrosion chemistry: a focus on anodic hydrogen evolution on Al and Mg, Faraday Discuss 180 (2015) 11–33, https://doi.org/10.1039/C5FD00066A.

[39] M. Curioni, P. Skeldon, E. Koroleva, G.E. Thompson, J. Ferguson, Role of tartaric

acid on the anodizing and corrosion behavior of AA 2024 T3 aluminum alloy, J. Electrochem. Soc. 156 (2009) C147–C153, https://doi.org/10.1149/1.3077602.
[40] Y.W. Ma, J.W. Choi, K.B. Yoon, Change of anisotropic tensile strength due to amount of severe plastic deformation in aluminum 2024 alloy, Mater. Sci. Eng. 529 (2011) 1–8, https://doi.org/10.1016/j.msea.2011.08.015.
[41] W.J. Stępniowski, M. Michalska-Domańska, M. Norek, E. Twardosz, W. Florkiewicz, W. Polkowski, D. Zasada, Z. Bojar, Anodization of cold deformed technical purity aluminum (AA1050) in oxalic acid, Surf. Coating. Technol. 258 (2014) 268–274, https://doi.org/10.1016/j.surfcoat.2014.09.013.
[42] G.E. Thompson, H. Habazaki, K. Shimizu, M. Sakairi, G.C. Wood, P. Skeldon, X. Zhou, Anodizing of aluminium alloys, Aircraft Eng. Aero. Technol. 71 (1999) 228–238, https://doi.org/10.1108/00022669910270709.